The (p,n) charge-exchange reaction on ^{90}Zr at intermediate energies

Rudolf T. Kabutz
Department of Physics
University of Cape Town

Submitted to the Faculty of Science in fulfillment of the requirements for the degree of Masters of Science

September 21, 1992

Abstract

Using the Time-of-Flight facility at the National Accelerator Centre at Fauré, the (p, n) charge-exchange reaction has been studied at intermediate energies of 120, 160 and 200 MeV, and at angles of 0°, 2° and 4°. In this work the data collected for the ^{90}Zr target will be presented. The influence on the data from slow neutrons due to previous pulses is discussed and the best manner of removing them from the spectra is recommended. It is shown how the background cosmic rays can be utilised to measure the intrinsic resolution of the detectors and to obtain an estimate of the neutron energy threshold. The differential cross-sections for the states corresponding to Fermi and Gamow-Teller transitions were extracted from the time spectra. The sum of the strength of all the discrete Gamow-Teller states was determined and compared to the Ikeda Sum Rule. It was found that only 50% of the sum could be accounted for in the discrete states. An overview of the theory that has been developed to extract Gamow-Teller strengths from the (p, n) cross-sections is given. Some of the theoretical models that have been used to describe the $^{90}Zr(p, n)^{90}Nb$ reaction and account for the missing Gamow-Teller strength are briefly discussed.

Acknowledgements

Thanks to

- the Foundation for Research and Development for enabling the financing of the thesis and the research programme.
- the Technical Advisory Panel of the National Accelerator Centre for allocating beam time for the (p, n) experiments, and for the greatly valued service of the operators to provide the best possible proton beams,
- the Indiana University Cyclotron Facility for supplying the ^{90}Zr target,
- James Wanliss for marching into the lab at the most inappropriate times,
- Karin Newton and Lesley Jennings for bearing with my constant, annoying presence in the office,
- Prof. Frank Brooks for always being willing to provide advice on the (unclear) nuclear physics,
- Jenny Bremer, who so efficiently ensured that the required reading material was available,
- the company of the mob: David, Rory, Ingrid, Rob, Eileen, Shaun, Kevin, Trevor and Janet,
- all the helpful hidden hands.
- my dad and my mom (for the countless cups of tea late at night),
- Karin for keeping an eye on me.
- the friendship of my collaborators: Peter, Richard, Victor and Douw (to him an additional thanks for sharing his territory with me and for his valuable critique of this document),
- most of all: Prof. David Aschman for his guidance in the thesis and for the joyful relationship over the past years.

Contents

List of Figures

List of Tables

Chapter 1

Introduction

Since 1989 a program studying the (p,n) reaction has been proceeding at the National Accelerator Centre near Fauré, Cape Town. The neutron time-of-flight spectrometer required for studying this charge-exchange reaction was fairly easily constructed. A $^{90}Zr(p,n)$ measurement could provide data for comparison to previous work to establish the accuracy of the neutron time-of-flight spectrometer. One might then proceed to investigate nuclei on which the (p,n) reaction had not been studied.

There is interest in studying the (p,n) reaction on medium mass nuclei, both of even and of odd mass. This is because the strength of the Gamow-Teller (GT) transitions is of interest, and in medium mass nuclei the Gamow-Teller strength is concentrated in a clearly distinguishable giant Gamow-Teller resonance. In light mass nuclei, however, the GT strength is fragmented, and in heavy mass nuclei the GT giant resonance lies close to the Isobaric Analog State.

So far the data of an odd-A nucleus has been studied by Tshivhase [TSH 92]. In the odd-A nuclei the difficulties in determining the ratio of the Fermi to the Gamow-Teller strength arise because of a mixture of both Fermi and Gamow-Teller strength in the Isobaric Analog State. This does not occur for even-A nuclei.

In this thesis the data obtained in the $^{90}Zr(p,n)^{90}Nb$ reaction will be presented and its analysis discussed. The ^{90}Zr nucleus is of particular interest for a number of reasons:

- in terms of the shell-model, a minor closure occurs at Z=40 and a major closure at N=50. Hence theoretical calculations for this nucleus become much simpler than for other nuclei,
- the Isobaric Analog State can be seen clearly separated from the other Gamow-Teller states, so the Fermi strength can be extracted unambiguously,
- a number of discrete Gamow-Teller states, as well as the Gamow-Teller Giant Resonance, which are known to have an $L = 0$ angular distribution, feature at low excitation energies and can be used to extract the sum of the Gamow-Teller strength in the discrete states,

- our measurements at NAC can be compared to previous work on the same nucleus to examine the accuracy of our neutron spectrometer,
- estimates of the Gamow-Teller strength in the continuum may be made by analysing the angular distributions of neutron spectra at high excitation energies, but for this further measurements at higher angles are required.

This thesis is laid out in the following way. Chapter 2 begins with a presentation of the reasons for interest in the (p,n) reaction. Then a short overview of relevant theory and information about the ^{90}Zr nucleus will be given. Specifically, the Ikeda Gamow-Teller sum rule will be shown, and a brief discussion of the possible reasons for missing strength in experimental studies.

In chapter 3 the experimental facilities used to acquire the data are described. The major factors contributing to the overall energy resolution of the neutron time-of-flight spectrometer are discussed. Then the method of recording specific events is described.

The analysis of the recorded events follows in chapter 4. The main task was to extract the number of neutron events from the time spectra corresponding to specific transitions.

The extracted counts for each peak in the spectrum are converted to differential cross-sections in chapter 5. Then the strengths of the Gamow-Teller states are calculated and summed, and compared to the Ikeda sum rule.

Conclusions are reached in chapter 6. Our measured sum is compared to the Gamow-Teller sum from other (p,n) experiments, and recommendations for further work are given.

In the Appendix A the log of data on $^{90}Zr(p,n)$ that was recorded is shown.

Chapter 2

Theory and previous studies

2.1 Reasons for interest in (p, n)

The (p, n) reaction at intermediate energies has received considerable attention in the last two decades since it is a good probe of the spin-isospin excitations of nuclei, and because better techniques are available to measure the neutron energies accurately using the time-of-flight (TOF) method [GOO 79, GOO 80]. Experimentally the data can easily be obtained at 0°, which corresponds to small momentum transfer.

In these charge-exchange reactions at small momentum transfer only the isovector part ($T = 1$) of the effective interaction is selected [LOV 87]. The isoscalar ($T = 0$) excitations are not allowed in a charge-exchange reaction such as (p, n), but in (p, p'), for example, both isoscalar and isovector excitations are possible.

Useful calculations have been performed with the distorted-wave impulse approximation (DWIA). The cross-section can then be split into a reaction part and a nuclear structure part. If the reaction mechanism is fairly well known, then the structure information, such as the Gamow-Teller strengths and strength distribution, can be extracted from the experimental cross-sections.

With the availability of medium energy proton beams the regions which are energetically inaccessible to β-decay can be probed. When the (p, n) reaction is performed at small momentum transfer, it can be related to the β-decay as shown in section 2.4. The (p, n) reaction would relate to β^- decay, thus measuring the β^--strength, $S_{\beta-}$.

The (n, p) reaction, the inverse charge-exchange process to (p, n), can be used to measure the β^+-strength, $S_{\beta+}$. This strength should be nearly completely Pauli blocked in neutron rich nuclei, and its unblocking, especially in the fp-shell, has interesting consequences in stellar collapse [DRO 86, BER 87]. The fp-shell shell nuclei, eg. Fe, are abundant in the core of the supernova precursor. Inverse β-decay occurs during the collapse and a neutron star, or possibly even a black hole, is formed. The rates of these inverse β-decays have a great influence on the detailed dynamics of the collapse.

A simple model independent sum rule can be used to compare the predicted GT strength with that measured by experiment. This sum rule predicts the difference between the β^+-strength and the β^--strength.

Extracting cross-sections from narrow discrete states is reasonably unambiguous. Difficulty arises in extracting cross-sections of some resonances at high excitation energies, where the peaks are broad and are lying on a continuum of unknown shape. The $(^3He, t)$ charge-exchange reaction has been used in comparison with (p, n) to study the higher lying peaks. These two reactions have different background conditions, which should help to identify the broad states. Unfortunately each of these backgrounds is thus far not well understood, so the comparison of broad peaks is only of limited use. However, the emerging particle, the triton, is charged. Hence the standard techniques to measure particle energies can be used (which are unsuitable for uncharged neutrons) and the $(^3He, t)$ can be studied with high resolution in a spectrometer.

It will be shown that experimentally the sum rule could not be fulfilled. Theoretical proposals to account for this missing strength will be overviewed.

2.2 Nucleon-nucleon and nucleon-nucleus interactions

In the (p, n) reaction the incoming nucleon, a proton, interacts with a nucleus which is a complicated system of bound protons and neutrons. The model of the nucleus would be very simple if one would assume that the nucleons are noninteracting amongst themselves. Then the free (p, n) scattering data could be directly related to the observables of a nucleus with A nucleons [GOO 87]. In this simple picture the kinematics and spin dependence would be identical and the cross-section would equal A times the free (p, n) cross-section.

Such a simple model is modified by the binding effect of the nucleons and the electric repulsion of the charged protons in the nucleus. But in the charge-exchange reactions of complicated heavy nuclei some of these simple characteristics are still visible. The nuclear medium has two effects on the reactions:

- the waves of the incoming proton and the outgoing neutron are distorted due to the interaction with all the nucleons in the nucleus,
- the transition of a neutron to a proton is not allowed for certain states in the nucleus already occupied by a proton, so the low-momentum-transfer transitions are Pauli blocked.

The scattering of nucleons is often described by the transition operator (or t-matrix), t_{ip}, which is obtained from the free nucleon-nucleon (NN) interaction in the impulse approximation [LOV 81, KER 59].

The combination of all the nucleons in the nucleus can be examined by assuming an effective interaction, V_{ip}, between the projectile (p) and the i^{th} nucleon as

$$V_{ip} = V^C(r_{ip}) + V^{LS}(r_{ip})\boldsymbol{L}\cdot\boldsymbol{S} + V^T(r_{ip})S_{ip}(\hat{r}_{ip}) \qquad (2.1)$$

which is a sum of central(C), spin-orbit(LS) and tensor(T) terms, where each term $V^{C,LS,T}$ depends on isospin and the energy of the projectile. Explicitly [LOV 87] the

spin(S)- and isospin(T)-transfer properties of the V_{ip} are:

$$\begin{array}{lccccccc} (S,T) = & 0,0 & & 1,0 & & 0,1 & & 1,1 \\ V_{ip} = & V_0^C & + & V_\sigma^C \boldsymbol{\sigma}_i \cdot \boldsymbol{\sigma}_p & + & V_\tau^C \boldsymbol{\tau}_i \cdot \boldsymbol{\tau}_p & + & V_{\sigma\tau}^C \boldsymbol{\sigma}_i \cdot \boldsymbol{\sigma}_p \, \boldsymbol{\tau}_i \cdot \boldsymbol{\tau}_p \\ & +V^{LS} \boldsymbol{L} \cdot \boldsymbol{s}_p & + & V^{LS} \boldsymbol{L} \cdot \boldsymbol{s}_i & + & V_\tau^{LS} \boldsymbol{L} \cdot \boldsymbol{s}_p \, \boldsymbol{\tau}_i \cdot \boldsymbol{\tau}_p & + & V_\tau^{LS} \boldsymbol{L} \cdot \boldsymbol{s}_i \, \boldsymbol{\tau}_i \cdot \boldsymbol{\tau}_p \\ & & + & V^T S_{ip} & & & + & V_\tau^T S_{ip} \, \boldsymbol{\tau}_i \cdot \boldsymbol{\tau}_p \end{array} \tag{2.2}$$

This effective interaction is quite complicated, but it is simplified in the distorted-wave impulse approximation [TAD 87] in the limit of zero momentum transfer. Then the spin-orbit and tensor terms, and those with angular momentum transfer $L > 0$, are negligible. The important properties of the effective interaction can be understood by examining each of the components of equation 2.2 as a function of momentum transfer (q), projectile kinetic energy (T_p) and spin and isospin transfer S and T. Each term in V_{ip} can be related to an element t_{ip} in the t-matrix.

Now the energy dependence of only the central terms, shown in figure 2.1, will be examined. The most dominant term is the scalar-isoscalar part (V_0^C), but this is

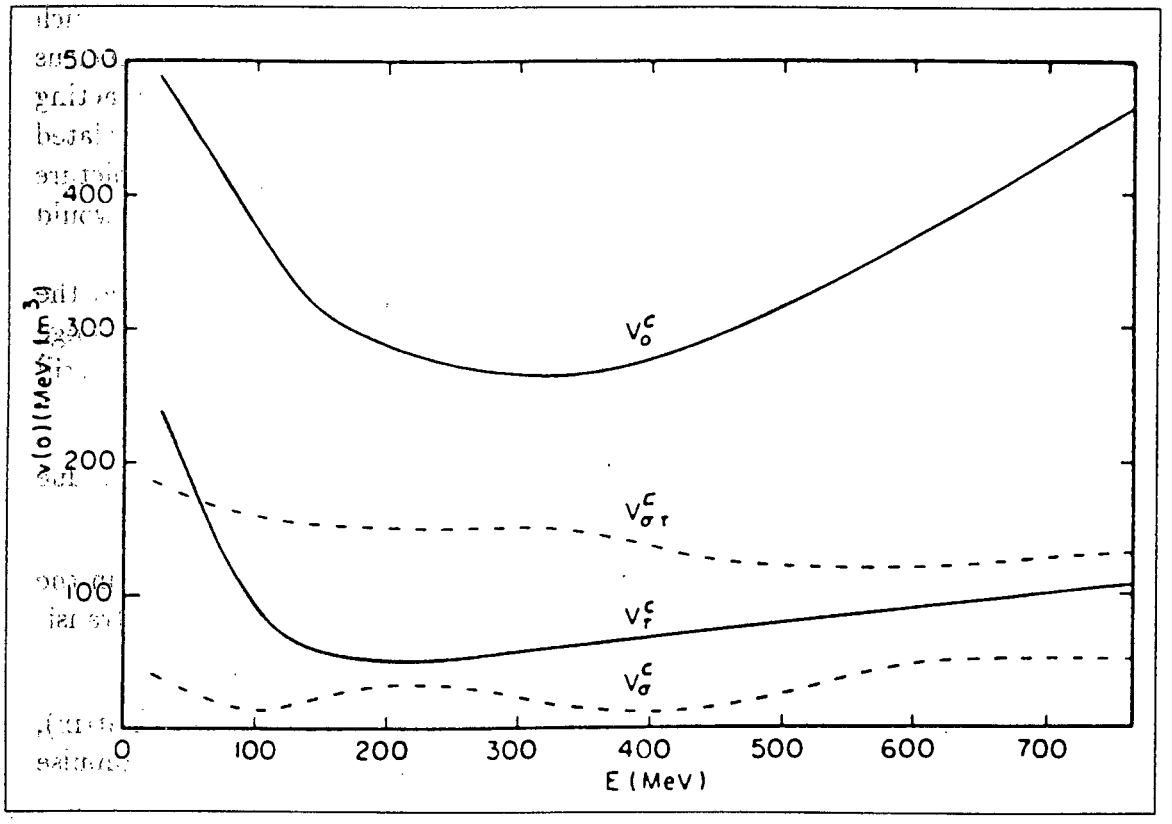

Figure 2.1: *Energy dependence of the central components of the effective t-matrix at zero momentum transfer. From [LOV 81].*

not present in the charge-exchange reactions. V_τ^C is strongly energy dependent, but $V_{\sigma\tau}^C$ and V_σ^C much less so. Thus when a particular nucleon bombarding energy is

selected, specific states can be excited due to the energy dependence of the various central components of V_{ip}.

2.3 Details about the $^{90}Zr(p,n)^{90}Nb$ reaction

The ground state of ^{90}Zr has $J^\pi = 0^+$ and $T = T_z = (N-Z)/2 = 5$, so by the (p,n) reaction some final state in the ^{90}Nb nucleus will be reached . On figure 2.2 the energy levels for three members of the A=90 isobar are shown. Of particular interest are the levels of ^{90}Nb reached by $^{90}Zr(p,n)$, as they can be compared to states seen in the experimental (p,n) spectra. The zero degree spectra for each of

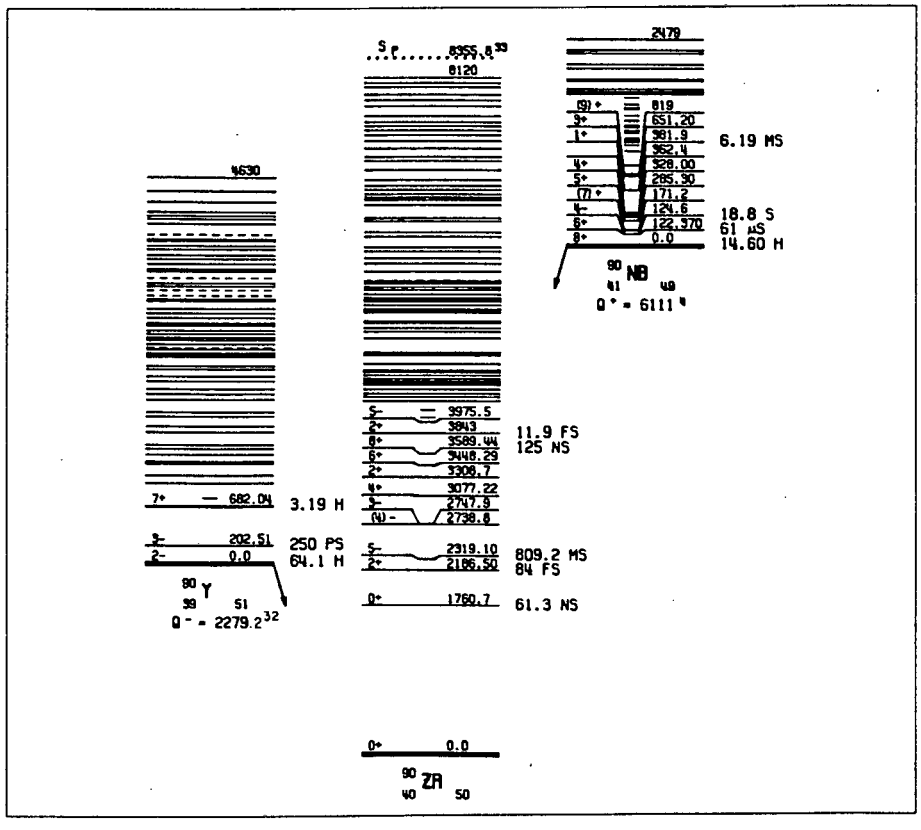

Figure 2.2: *Energy level diagram of three members of the A=90 isobar. Using* ^{90}Zr *as the target, the* (p,n) *reaction reaches the states of* ^{90}Nb *and the* (n,p) *reaction the states of* ^{90}Y. *From [HOR 75].*

the energies used are shown in figure 2.4 on an excitation energy scale. The GT transitions proceed from the ^{90}Zr target 0^+ ground state to 1^+ levels in ^{90}Nb. The detailed energy levels of ^{90}Nb, adopted from a number of reactions, are shown on figure 2.3. The only 1^+ level seen to correspond to a peak in the experimental spectrum is the 1^+ state at $E_x = 2.3089$ MeV. This state appears as a strong peak in the (p,n) spectra (labelled on the top spectrum in figure 2.4). Other 1^+ states

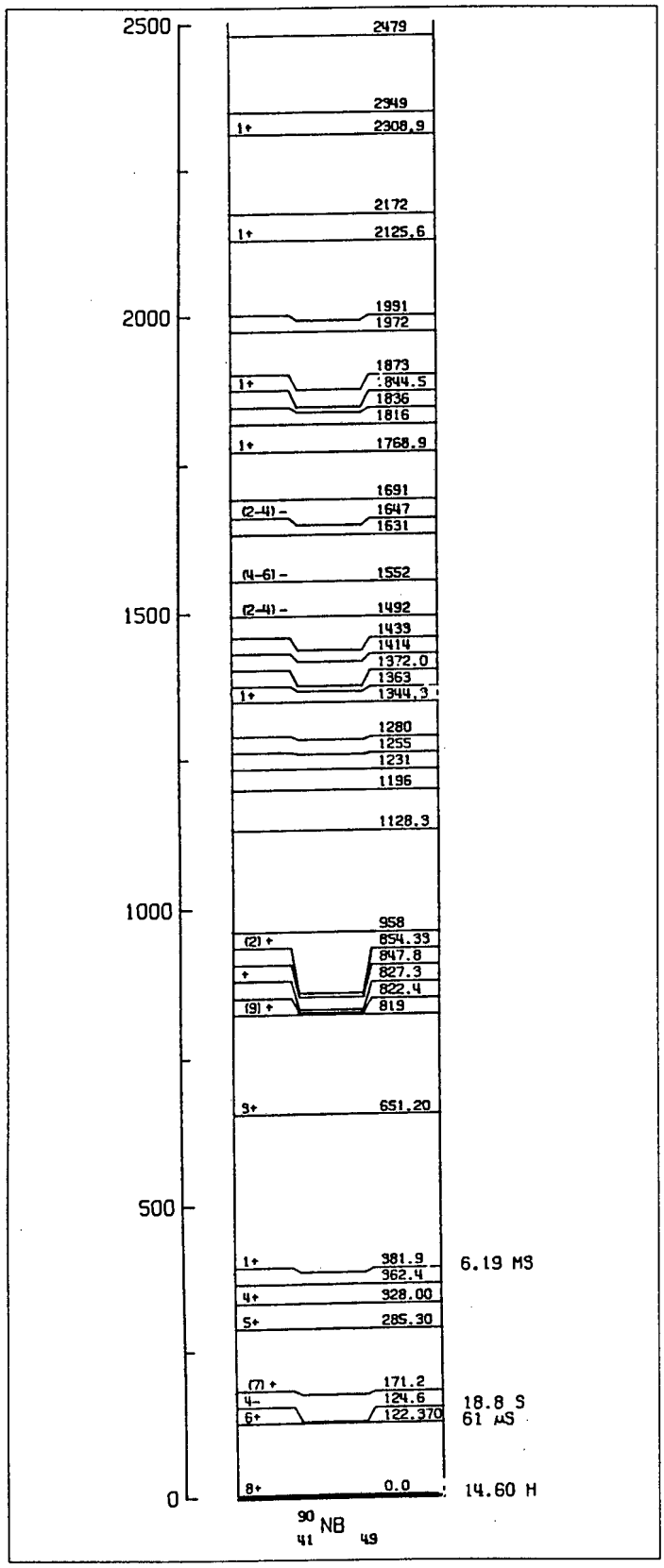

Figure 2.3: *Energy level diagram of ^{90}Nb. The 1^+ states can be reached via the GT transition from the ^{90}Zr ground state. From [HOR 75].*

(down to about 1.70 Mev) may also contribute to this peak, but with our resolution of ~600 keV the they would indistinguishable.

There is no level corresponding to the small $E_x = 0.9$ MeV state observed in the spectra. This small peak is thought to be a combination of low-lying unresolved 1^+ levels. No levels for $E_x \geq 2.5$ MeV are listed on the published energy level diagram. A number of interesting features can be seen in the (p,n) spectra (labelled on the 120 MeV spectrum on figure 2.4):

- the Isobaric Analogue State (IAS), which is reached by the Fermi transition from the 0^+ target ground state to a 0^+ state in the daughter nucleus, and lies at an excitation energy (E_x) of ~5.1 MeV with a narrow width,
- the Gamow-Teller 1^+, $T = 4$ type states, of which some appear as narrow discrete peaks at low excitation energy, while others combine to form the Gamow Teller giant resonance (GTGR) at E_x ~8.7 MeV with a full width at half maximum (FWHM) of 4.4 MeV,
- a Gamow-Teller transition to a $T = 5$ state at $E_x = 13.4$ MeV with FWHM = 3.1 MeV and
- an $L = 1$ distribution at high excitation energy of ~18 MeV.

In comparing the (p,n) spectra of figure 2.4, it can be seen that as the proton energy increases, the strength of the F transition (to the IAS) decreases, and of the GT transitions increases. This is in accordance with the overall trend that F transitions strongly dominate spectra at low energies of $E_p \leq 45$ MeV and the GT transitions dominate at high energies of $E_p \geq 100$ MeV [GOO 80]. An overview of previous measured quantities for each of these transitions will now be given.

2.3.1 The isobaric analogue state

The Fermi operator connects the 0^+ ground state in the parent nucleus to a unique 0^+ state in the daughter nucleus. Hence all the Fermi strength is concentrated in that state, and the neutrons from the Fermi transition have a unique energy. Thus the measured width of the IAS is not due to a spreading in neutron energies in the Fermi transition, but only due to the experimental resolution. The transition produces a change in the projection of the isospin ($\Delta T_z = \pm 1$), but not a change in the total isospin ($\Delta T = 0$) or the spin ($\Delta S = 0$). The energy of the IAS can be given by an empirical formula fitted to the position of the IAS for many medium-A nuclei [TAD 87]

$$\begin{aligned} E_x(IAS) &= \omega_{\mathrm{IAS}} + Q_{\mathrm{ground\,state}} \\ &= 0.722(2Z+1)A^{-1/3} - 1.13 - 6.893 \text{ MeV} \end{aligned} \tag{2.3}$$

where Z is the atomic number of the target nucleus. This energy of 5.03 MeV from the formula lies reasonably close to the measured value of 5.14 MeV [HOR 75].

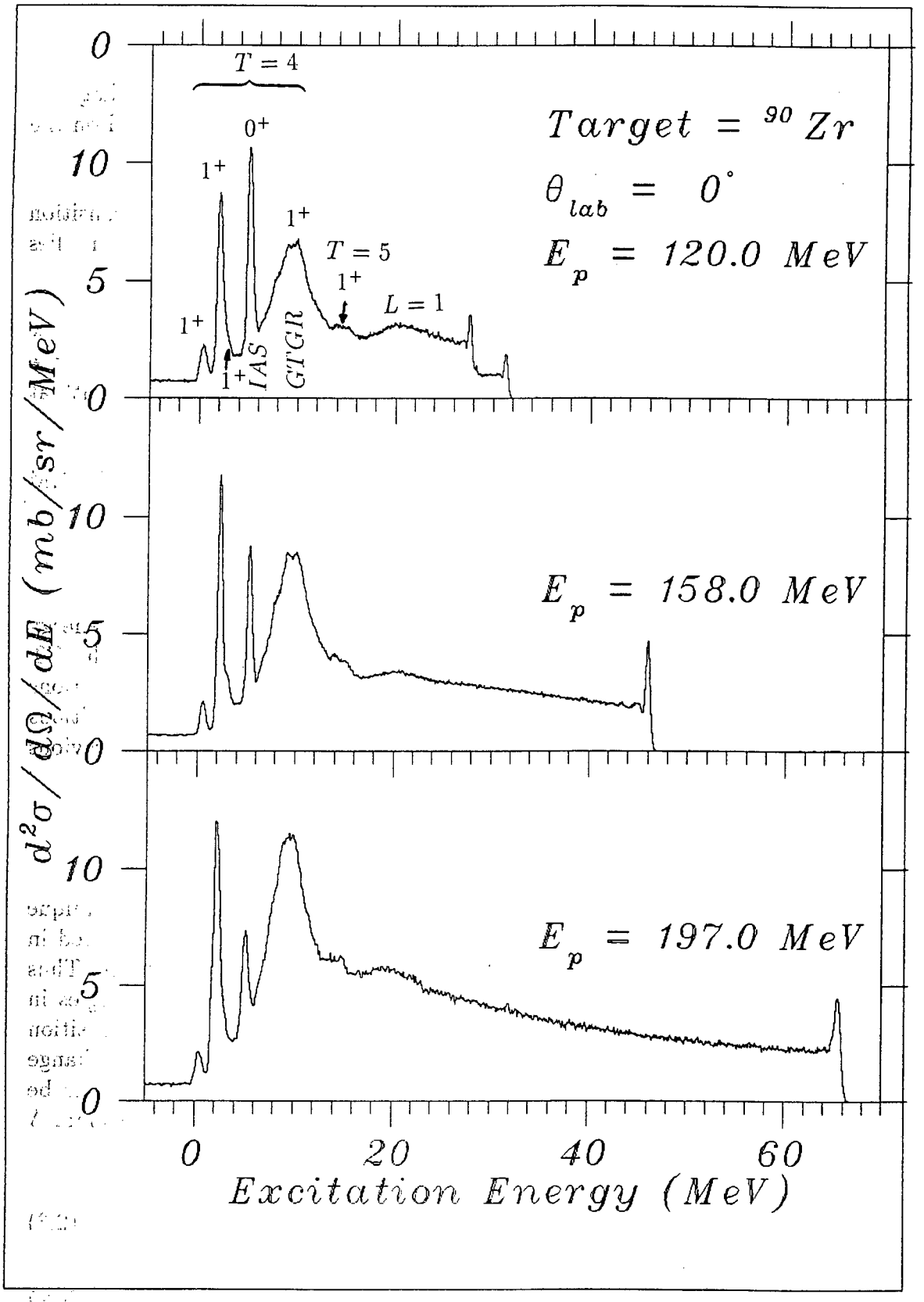

Figure 2.4: *Excitation energy spectra at E_p = 120, 160 and 200 MeV at zero degrees. The interesting features labelled on the top spectrum are explained in the text.*

2.3.2 The Gamow-Teller giant resonance

The concentration of GT strength in a peak at high excitation energy was proposed by Fujita *et al.* [FUJ 64, IKE 63] to explain the hindrance of β-decay in medium and heavy mass nuclei. This resonance was first observed by Doering *et al.* [DOE 75] in the (p,n) reaction on ^{90}Zr at $25 \leq E_p \leq 45$ MeV. In the $^{90}Zr(^3He,t)$ reaction in 1975 this broad peak was also seen [BLA 76]. Since the angular distribution of the GTGR is similar to lower lying 1^+ states, it was also assigned 1^+ by Doering *et al.* [DOE 75]. The GTGR is excited by the $V^C_{\sigma\tau}\boldsymbol{\sigma}\cdot\boldsymbol{\sigma}\ \boldsymbol{\tau}\cdot\boldsymbol{\tau}$, and from about 100 MeV upwards this resonance becomes a very prominent feature in the 0° spectra.

The energy separation between the GTGR and the IAS was predicted to be linear in $(N-Z)/A$ [IKE 63, FUJ 64]. From experimental data the separation was determined by Horen *et al.* [HOR 81] as

$$E_{GTGR} - E_{IAS} = 6.7 - 60T\,A^{-1} \tag{2.4}$$

and later with more available data by Nakayama *et al.* [NAK 82] as

$$E_{GTGR} - E_{IAS} = 26A^{-1/3} - 37T\,A^{-1} \tag{2.5}$$

where $T = (N-Z)/2$. The second formula fitted the data much better. It shows that for nuclei with small neutron excess the first term ($A^{-1/3}$) dominates and the GTGR lies above the IAS. But for heavy nuclei, the second term balances the first and the GTGR is at the same energy as the IAS. The energy separation between the GTGR and the IAS of 3.7 MeV from the formula agrees well with the experimental energy separation of 3.6 MeV.

2.3.3 Other Gamow-Teller peaks

At low excitation energies a strongly excited state can be seen at $E_x = 2.3$ MeV, a smaller peak features at ~0.9 MeV, and another small one at ~3.0 MeV, seen as a shoulder on the 2.3 MeV state. These three states result from transitions to states with $J^\pi = 1^+$ and $T = 4$. A broad peak at $E_x = 12.5$ MeV can be seen in the spectra. The strength of this peak is very similar to that of shell model calculations which show a $T = 5$ state at the same position [MAT 83].

2.3.4 Higher multipole transitions (L>0)

A resonance with an $L = 1$ angular distribution was found at $E_x = 17.9$ MeV [BAI 80]. This feature is however not unique to a single target, but has been seen in spectra from ^{90}Zr to ^{208}Pb. The typical width is ~10 MeV and the E_x ~20 MeV [BER 81]. From studies on numerous targets with A≥90 [HOR 81] the energy difference between $L = 1$ resonances and the IAS was found to be linear in $(N-Z)/A$

$$E_{\Delta L=1} - E_{IAS} = 13.6 - 66.0T\,A^{-1} \tag{2.6}$$

with $T = (N-Z)/2$ again.

Even at $E_p = 200$ MeV the resonance remains. At this energy the $S = 0$ transfer is greatly suppressed, and so it is assumed that it is a spin flip, $S = 1$, transition [CHA 81]. When $S = 1$ is coupled to $L = 1$, then the individual states can have $J = 0, 1, 2$. In theoretical studies on ^{208}Pb, Krmpotić *et al.* [KRM 80] have shown that $J = 0$ states have the highest energy, $J = 0$ and $J = 1$ have nearly all strength in the same state and for $J = 2$ the strength is spread over several states. Similar features were obtained in calculations by Cha *et al.* [CHA 81] of the $L = 1$ strength distribution of the various J states in ^{90}Zr. These strength functions were smoothed with Lorentzian curves and compared to experiment: a broad peak, as observed in experiment, occurs at about 20 MeV, but the large $L = 1$ component at lower excitations energies has not been seen in experiments.

In measurements of angles up to $\sim 48°$ at $E_p = 200$ MeV, Gaarde *et al.* [GAA 81] observed an $L = 2$ peak at $E_x \sim 24$ MeV, with a width of 14 MeV. This peak corresponds to the transition $f_{5/2} \rightarrow h_{11/2}$. Its maximum is at $\theta = 10°$, so in our available spectra at small angles up to 4° this transition cannot be seen.

2.3.5 The high E_x continuum

The continuum at high excitation energies is of interest, since a significant portion of the GT strength, which has not been measured in the discrete peaks, could be hidden there. The continuum is featureless, and its shape and magnitude are not well understood. Many suggestions have been made how the strength could be shifted to higher excitation energy, and how this strength could possibly be found. These points will be presented in section 2.6.

2.4 Fermi and Gamow-Teller transitions

The most interesting terms in the effective interaction (equation 2.2) are the central isovector ($T = 1$) terms. They can be related directly to the β-decay operators [TAD 87]. The non-spin-flip ($S = 0$) corresponds to Fermi β-decay

$$\sum_i V_\tau \boldsymbol{\tau}_i \cdot \boldsymbol{\tau}_p \iff G_V \sum_i \boldsymbol{t}_i^{\pm} \tag{2.7}$$

and the spin-flip ($S = 1$) to Gamow-Teller β-decay

$$\sum_i V_{\sigma\tau} \boldsymbol{\sigma}_i \cdot \boldsymbol{\sigma}_p \, \boldsymbol{\tau}_i \cdot \boldsymbol{\tau}_p \iff G_A \sum_i \boldsymbol{\sigma}_i \boldsymbol{t}_i^{\pm} \tag{2.8}$$

where in the β-decay operators G_V and G_A are the polar vector and axial-vector coupling constants respectively, $\boldsymbol{t}^{\pm}$ is the (single-particle) isospin raising or lowering operator, and $\boldsymbol{\sigma}$ is the intrinsic spin operator [WON 90]. For even-A, $T \neq 0$ targets, with 0^+ ground state, these decays would be $0^+ \rightarrow 0^+$ and $0^+ \rightarrow 1^+$ respectively [TAD 81].

It is useful to define the $B(F)$ and $B(GT)$, which are nuclear F and GT strength functions. More precisely, they are the F and GT reduced transition probabilities averaged over initial states and summed over those final states not distinguished in

the experiment, and summed over nucleons by the nucleon operator [GOO 87]. For F transitions this would be [TAD 81]

$$B(F) = \frac{1}{2J_i+1} \sum_{\mu} |\langle f || \sum_{k=1}^{A} \tau_\mu(k) || i \rangle|^2 \qquad (2.9)$$

and for GT transitions

$$B(GT) = \frac{1}{2J_i+1} \sum_{\mu} |\langle f || \sum_{k=1}^{A} \sigma_\mu(k)\tau_\mu(k) || i \rangle|^2 \,. \qquad (2.10)$$

For ^{90}Zr the ground state is 0^+, so $J_i = 0$. Usually $B(GT)$ and $B(F)$ are given in units of $g_A^2/4\pi$ [GAA 81]. Then for a free neutron in the initial state, and a free final proton, one would obtain [GOO 87]

$$\begin{array}{llll} B(F)^- & = 1 & B(F)^+ & = 0 \\ B(GT)^- & = 3 & B(GT)^+ & = 0\,. \end{array} \qquad (2.11)$$

All the Fermi strength is concentrated in the IAS, so $B(F) = N - Z$ for that state, and is zero for all other states. However, the $B(GT)$ is distributed over many states. In particular, the strength in the IAS is *pure* Fermi for even-A nuclei, but is a *mixture* of F and GT in odd-A nuclei. The fraction of GT in the IAS can be calculated making use of the ratio R which will be defined below (equation 2.18). A collaborator, V.Tshivhase [TSH 92], obtained the fraction of GT in the IAS for the $^{51}V(p,n)^{51}Cr$ reaction as ~0.04 for E_p=120–200 MeV. So also in this odd-A nucleus the fraction of F is close to unity.

The sum of $B(GT)$ is called the total Gamow-Teller strength, ie. $\sum_i B(GT) = S_\beta$. A sum rule for the total GT strength proposed in 1963 by Ikeda *et al.* [IKE 63, GAA 80] has been used extensively in these charge-exchange reactions.

This model-independent sum rule is [GAA 81, WON 90]

$$\begin{aligned} S_{\beta^-} - S_{\beta^+} &= \sum_f \sum_\mu |\langle f | \sum_{k=1}^{A} \sigma_\mu(k)\tau_-(k) | i \rangle|^2 \\ &\quad - \sum_{f'} \sum_\mu |\langle f' | \sum_{k=1}^{A} \sigma_\mu(k)\tau_+(k) | i \rangle|^2 \\ &= 3(N-Z) \end{aligned} \qquad (2.12)$$

where the σ_μ are the spherical components of the spin operator.

If all the nucleons were completely free this sum rule would hold [GOO 87]. Then all the neutrons would be available for β^- decay, and at equation 2.11 it was shown that $B(GT)^- = 3$ for a free neutron, so the total β^- strength for the nucleus would be $3 \times N$. In the same way the β^+ decay for protons would give $3 \times Z$, giving $S_{\beta^-} - S_{\beta^+} = 3(N-Z)$. However, the nucleons are not independent, and in a nucleus with neutron excess, this inverse β decay would be strongly Pauli blocked, resulting

in $S_{\beta+} \sim 0$. Using the $^{90}Zr(n,p)$ reaction, the magnitude of $S_{\beta+}$ can be measured, and if its contribution is small, then $S_{\beta-} \sim 3(N-Z)$ [GOO 87, DRO 86]. Even if the $S_{\beta+} > 0$, then $3(N-Z)$ is still a lower limit for the $S_{\beta-}$. Here the discrepancy with experiment arises: for nuclei over a large mass range only about 50% of this sum rule has been measured. A compilation of the summed strength for many nuclei has been given by Gaarde [GAA 85].

2.5 Strength obtained from cross-sections

The information we obtain from the experimental neutron spectra is the cross-section. We want to use this to get information about the nucleus. The cross-section depends on a number of factors [TAD 87]: the projectile energy (Ep), the number and type of nucleons in the target A(N,Z), the energy loss $\omega = E_x - Q_{g.s.}$ and the specific nuclear structure relationship between initial and final states. So the cross-section can be written as

$$\sigma = \hat{\sigma}_\alpha(E_p, A)\, F_\alpha(q,\omega)\, B(\alpha) \tag{2.13}$$

where α is F ($S=0, T=1$) or GT ($S=1, T=1$) and the $\hat{\sigma}$ is the unit cross section (a proportionality factor), F is a form factor describing the shape of the cross-section and B is the β decay transition strength.

Using standard direct-reaction theory, the differential cross-section can be calculated [KER 59] in the following manner

$$\sigma = \frac{E_i E_f}{(2\pi\hbar^2 c^2)^2}\frac{k_f}{k_i}\frac{1}{2(J_i+1)}\sum |T(M_F M_I m_p m_n)|^2 \tag{2.14}$$

where $E_i(E_f)$ is the initial (final) reduced energy and the sum is over the spin projections of the projectile and the target. By using the transition matrix, T, in the distorted-wave approximation, applying simplifications for small momentum transfer and using the eikonal approximation for the distortion factors, the cross-section [TAD 87] can be written as

$$\sigma(q,\omega) = K(E_p,\omega)|J_{ST}|^2 \exp(-\frac{1}{3}q^2\langle r^2\rangle) \exp(-xA^{1/3} + p(\omega))\, B(ST) \tag{2.15}$$

where a kinematic factor has been defined as

$$K(E_p,\omega) = \frac{E_i E_f}{(2\pi\hbar^2 c^2)^2}\frac{k_f}{k_i}$$

and the J_{ST} is the Fourier Transform of the relevant effective nuclear interaction component, either t_τ or $t_{\sigma\tau}$ [TAD 81].

Previously Goulding *et al.* [GOU 80] defined the cross-section as

$$\sigma(q,\omega) = K(E_p,\omega)\, N_{ST}^D\, |J_{ST}|^2\, B(ST) \tag{2.16}$$

where the ratio of the plane-waves and distorted-waves cross-section is called the distortion factor

$$N^D(q,\omega) = \frac{\sigma(DW;q,\omega)}{\sigma(PW;0)} \,. \tag{2.17}$$

Taddeucci *et al.* [TAD 87] compared the differential cross-section (equation 2.15) to full DWIA calculations. They found that the simple model for $J^\pi = 0^+$ and 1^+ transitions agrees very well with the calculations which also include non-central interaction, $L \neq 0$ amplitudes and reasonable optical parameters. The data for five targets has been plotted on figure 2.5.

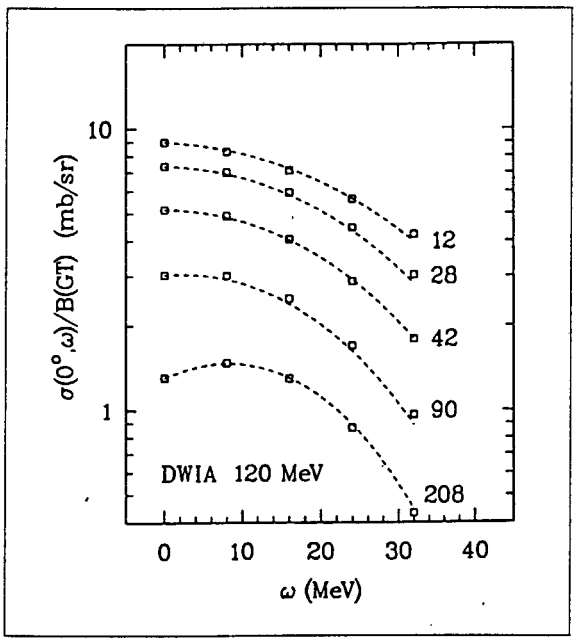

Figure 2.5: *Comparison between the full DWIA calculation cross-sections (squares) and the model cross-section (dashed line). The data for five masses at $E_p = 120$ MeV is plotted against energy loss. From [TAD 87].*

To calculate the B(GT) for ^{90}Zr, the ratio of the unit cross-sections R^2 can be used

$$R^2(E_p,A) = \frac{\hat{\sigma}_{GT}(E_p,A)}{\hat{\sigma}_F(E_p,A)} \,. \tag{2.18}$$

From equation 2.13, but using the kinematic factor $K(E_p,\omega)$ instead of the full correction factor $F(q,\omega)$ this ratio, for even-A nuclei, can be written in terms of the experimental cross-section, σ_F and σ_{GT}, as

$$R^2 = \frac{\sigma_{GT}(0°)}{\sigma_F(0°)} \frac{(N-Z)}{B(GT)} \frac{K(\omega_0)}{K(\omega_1)} \,. \tag{2.19}$$

For odd-A nuclei R has to be slightly modified: then the cross-sections for the mixed IAS (Fermi and Gamow-Teller contributions) and a nearby pure GT transition are

used. This ratio R can be interpreted as

$$R \approx \frac{|J_{\sigma\tau}|}{|J_\tau|}\left(\frac{N_{\sigma\tau}}{N_\tau}\right)^{1/2} . \tag{2.20}$$

At intermediate energies of 80–200 MeV, in which we are interested, the DWIA shows that the distortion factor ratio $N_{\sigma\tau}/N_\tau$ is almost independent of energy and $N_{\sigma\tau}/N_\tau \sim 1.2 \pm 0.1$ for GT and F transitions not widely separated in energy [TAD 81]. Hence R very nearly equals the ratio of the interaction strengths $|J_{\sigma\tau}/J_\tau|$ at $q \sim 0$. The significance of this R^2 is [GOU 80] that it measures the effectiveness of the (p,n) reaction in producing spin-flip transitions relative to non-spin-flip transitions.

The ratio R has been measured experimentally from cross-sections for many even-A targets with $N - Z \neq 0$. To do this, targets for which β decay lifetimes were known had to be used. The β decay transition strengths were then calculated [WIL 80] from the β decay lifetimes by using

$$B(F) + (1.260 \pm 0.008)^2 B(GT) = \frac{6166 \pm 2sec}{ft} \tag{2.21}$$

with the coupling constants from Wilkinson [WIL 82]. The values measured for $R(E_p)$ have been plotted on figure 2.6, where equation 2.19 was used to calculate R for the even-A nuclei in the top graph in the figure, and a modified equation for the odd-A nuclei in the bottom graph. From the figure it can be seen that $R(E_p)$ shows a mass dependence for $E_p < 50$ MeV. The possible causes for this are [TAD 81]: the effects of compound nucleus and shape resonances, channel coupling, multistep reactions or other nondirect effects which are most significant at lower energies. However, in the energy range $50 \leq E_p \leq 200$ MeV the curve of R is remarkably linear (as in figure 2.6). Taddeucci *et al.* [TAD 87] concluded that $R(E_p)$ is a universal characteristic of (p,n) scattering.

So R can be obtained from the linear relationship $R(E_p) = E_p/E_0$ with $E_0 = 55.0 \pm 1.7$ MeV for even-A and thus the GT unit cross-section can be calculated for targets with $N - Z \neq 0$ by

$$\hat{\sigma}_{GT} = \frac{(E_p/E_0)^2}{F(q_0,\omega_0)}\frac{\sigma_F(0°)}{(N-Z)} = \left(\frac{E_p}{E_0}\right)^2 \hat{\sigma}_F . \tag{2.22}$$

Once the GT strength has been calculated for all $(GT)^-$ states, it can be summed for all those states, giving $S_{\beta-}$, and compared to the Ikeda Sum Rule.

2.6 The missing Gamow-Teller strength

The simple model independent sum rule proposed by Ikeda states that a lower limit for the sum of Gamow-Teller strength is $S_{\beta-} - S_{\beta+} = 3(N - Z)$. In many nuclei all over the periodic table this sum rule not be satisfied by the strengths extracted from experimental cross-sections. Assuming that the $S_{\beta+}$ strength is small for neutron

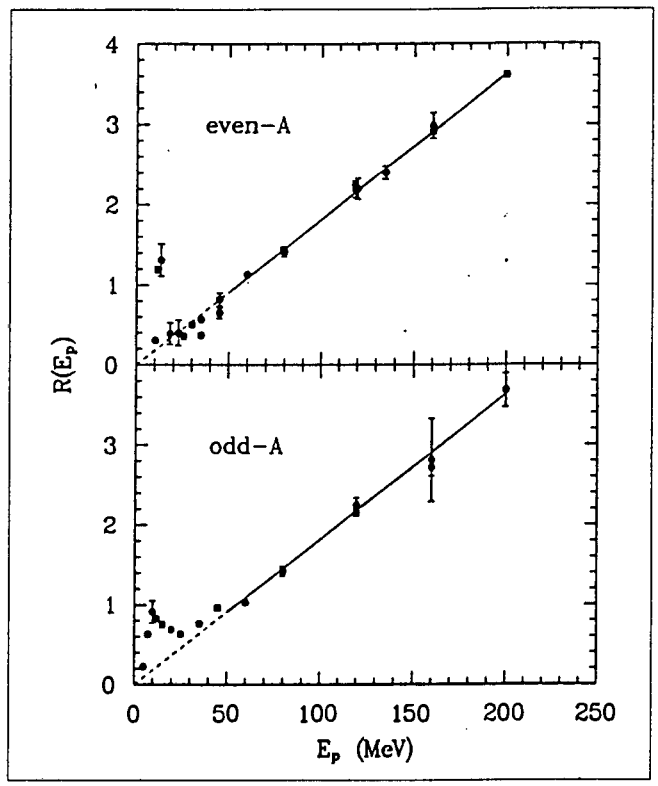

Figure 2.6: *The ratio R of unit cross-sections calculated from experimental cross-sections for many even-A and odd-A nuclei. From [TAD 87].*

rich nuclei, the lower limit for $S_{\beta-}$ would be $3(N-Z)$. For A$\geq$ 90, only 50-60% of the expected $S_{\beta-}$ has been measured.

There is still an open question as to how much of the strength is in the background underneath the discrete peaks, or in the continuum at excitation energies above the GTGR. Two main proposals have been made to explain the missing strength:

1. that $\Delta(1232)$-isobar–nucleon-hole (Δ-h) couple to proton-particle–neutron-hole (pn^{-1}) states with the GT operator, which removes some of the strength to higher excitation energy [RHO 74, OST 82].

2. that ordinary nuclear configuration mixing, such as between two-particle–two-hole (2p-2h) states and 1p-1h GT states, also shifts strength to higher excitation energies [SHI 74].

There have been many calculations for each of the two proposals. An extensive review of progress thus far has been given by Bertsch, *et al.* [BER 87], and Osterfeld [OST 92].

2.6.1 Delta excitations

In this mechanism the internal degrees of freedom of the nucleon, identified specifically as the Δ-isobar excitations of the nucleon [RHO 74], move GT strength from low excitation energy to higher excitation energy. The way in which the GT modes are coupled to internal nuclear excitations can be considered as a spin-isospin flip transition of a quark in the nucleon [OST 85].

The effect of these Δ-h excitations can be calculated using the random-phase approximation (RPA) [CHA 81]. Then, instead of introducing particle-hole configurations, rather Δ-hole configurations are used [BER 87]. The magnitude of this mechanism in quenching depends strongly on the coupling between the p-h states with the Δ-h states. The results of this have important consequences for the understanding of the role of Δ's in nuclei [OST 85].

2.6.2 Configuration mixing

In this process higher-lying 2p-2h states mix with 1p-1h states and shift GT strength to excitation energies much higher than the GTGR [OST 92]. The magnitude of this effect on the quenching also depends on the coupling strength, here between the 1p-1h and 2p-2h states.

If configuration mixing is a major contribution to the quenching, then the GT strength lies beyond as well as below the GTGR. It thus becomes very difficult to detect, because in the 0° spectra the continuum is featureless.

There have, however, been attempts to extract the GT strength from the continuum. At high excitation energies values of the GT strength can be obtained by: calculating the physical background in terms of single quasi-free scattering, subtracting it from the spectrum and then analysing the residual spectrum for GT strength by performing a multipole decomposition. This method has been used [GAA 81, AND 85, AND 90] to obtain better limits for $E_x < 50$ MeV.

As an example, Scholten *et al.* [SCH 83] searched for $L = 0$ strength using this method on $^{90}Zr(p,n)$ data at $E_p = 200$ MeV. They used a quasifree background (calculated by Bertsch *et al.* [BER 82]) and a sum of $L = 0$, 1 and 2 angular distributions in the energy range $E_x = 15$ to 45 MeV. By extracting the $L = 0$ strength, they were able to account for about *half* of the missing strength. Note that $L = 0$ strength which might lie above $E_x = 50$ MeV cannot be extracted well, since even at 0° there is a large momentum transfer and the $L = 1$ distribution also becomes forward peaked.

One approach of addressing the question of how some of the missing strength has been shifted to higher excitation energy was taken by Drożdż *et al.* [DRO 86]. They show that conventional RPA results in two GT states due to the mixing between $\nu|g_{9/2} \rightarrow \pi|g_{9/2}$ and $\nu|g_{9/2} \rightarrow \pi|g_{7/2}$ transitions. When they allowed for 2p-2h mixing, they found significant spreading of the higher energy resonance. Of interest is that a tail developed towards the high excitation energies so that about 30% of the 3(N-Z) sum rule lay *above* $E_x = 21$ MeV.

The relative importance of these two processes of removing the GT strength has not been established conclusively. Various theoretical studies have provided differing results: for some the Δ excitations were of greatest importance, for others the configuration mixing, and for yet others both have a comparable quenching effect [BER 87].

In the next chapter details of the experimental apparatus which was utilised to acquire our data will be given. From this data the GT strengths will be extracted. The sum of the GT strength will be compared to the sum rule outlined above in this chapter.

Chapter 3

Experimental Apparatus

The (p, n) experiments were performed with the k=200 cyclotron at the National Accelerator Centre (NAC) near Fauré, Cape Town. The proton beam was sent by the light ion injector cyclotron (SPC1) into the separated sector cyclotron (SSC) and then transported to the N-line (on the lower right in figure 3.1). The targets

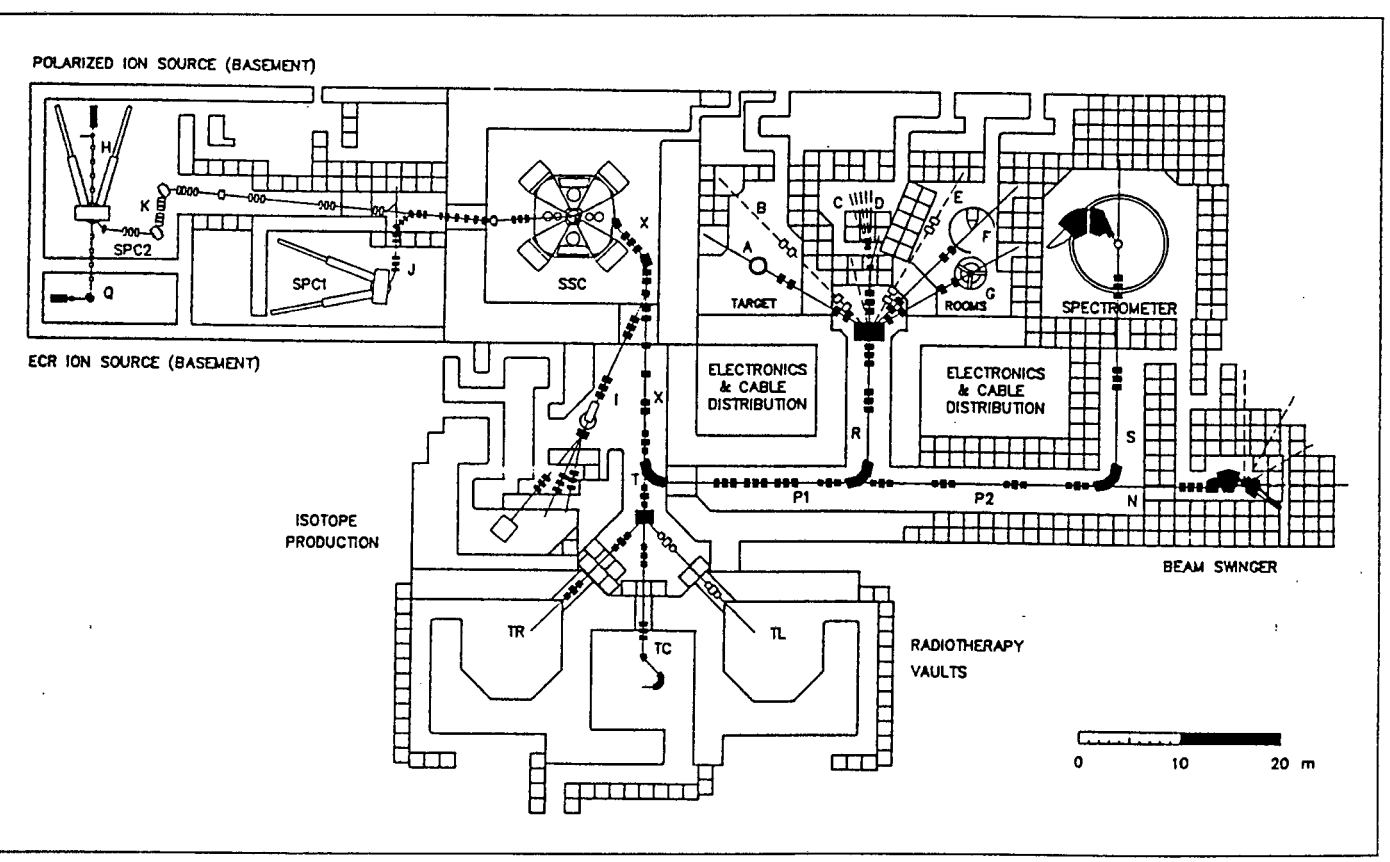

Figure 3.1: *Layout of the beamlines and shielding walls at NAC. The neutron time-of-flight facility is along the N-beam line. From [NAC 91].*

were situated in the beam swinger vault and the neutron detectors in a hut outside the main building in the neutron time-of-flight park (to the right of figure 3.1). The data analysed in this study was recorded during October/November 1990 and during June/July 1991. A log of the run data is listed in appendix A.

The beam currents that were used lie in the range 80–2000 nA. An average machine vacuum of 5×10^{-5} Pa [NAC 90] was maintained. The proton energies of 120, 160 and 200($\pm$0.1%) MeV were utilised. Neutrons were observed at angles of 0°, 2° and 4° relative to the incident proton beam. The event rate for the ^{90}Zr, 134 mg.cm^{-2} target for neutrons detected above threshold was $\sim$70 events/second, when the detectors were placed at 174 m from the target. The typical beam energy spread was 150 keV as discussed in section 3.2.2.

The experimental facilities that were used at NAC will be described in section 3.1. The aim of the time-of-flight method is to obtain as good a time resolution as possible, and hence an energy resolution as good as possible, to measure neutron energies. In section 3.2 the major contributions to the total energy resolution will be discussed. The electronics used to determine valid events and the apparatus used for recording the data will be outlined in section 3.3.

3.1 Experimental facilities used

3.1.1 Zirconium targets

Two self-supporting metallic ^{90}Zr foils were available. The one target of thickness 10.0 mg.cm^{-2} was used during the experimental sessions in 1990, while another of 134 mg.cm^{-2} was used in the 1991 sessions. Although the resolution of the data from the thinner target used in 1990 was much better than that for the latter, the statistics was much poorer due to the lower reaction rate because of the smaller target thickness. The 134 mg.cm^{-2} target was kindly supplied by the Indiana University Cyclotron Facility for use in the $^{90}Zr(n,p)$ experiment. For this reaction a high rate was required, thus such a thick target was used. So the 1990 data was used only to check the trends of the data at the later experimental session (ie. changes in the spectra with changes in energy and angle), but could not be used to extract reliable cross-sections. The isotopic purity of the thicker target used for the data presented in the analysis was 97.6%. The isotopic abundance of this ^{90}Zr target are listed in table 3.1. The targets were mounted in a movable target ladder with six positions. Of those one was used for a scintillating quartz viewer used for fine adjustment of the beam on the target, and another for the natural Li target used for efficiency measurements.

3.1.2 Neutron detectors

Each neutron detector consisted of a NE102A scintillator of dimensions 60 × 10 × 10 cm^3, viewed at each end by Hamamatsu R329 photomultiplier tubes (10 stage, 2″ diameter photocathode with E934 base), coupled by tapered perspex light guides. The components were connected with optical grease and each detector was housed

Table 3.1: *Isotopic abundances of the Zirconium target used in 1991.*

Isotope (Z)	*Atomic %*
90	97.62± 0.10
91	0.96 ± 0.05
92	0.71 ± 0.05
94	0.55 ± 0.05
96	0.13 ± 0.05

in a light-tight aluminium box. The height and width dimensions of the detectors had to be large enough to obtain a reasonable efficiency at the long flight path.

A vertical stack of 6 detectors was used. The stack was positioned transversely to the neutron beam, so the total frontal detection area was 60 × 60 cm^2. The depth of the detectors in the direction of the neutron beam is determined by two requirements [MAD 83]: it should be larger than the average range of charged reaction products from the neutron interactions in the detectors, and small enough so that the detector thickness does not contribute significantly to the flight path uncertainty.

The voltages for the photomultiplier tubes (PMT) were set at nominal values of −1500 V, and were adjusted roughly to match the amplitude spectra of all detectors.

3.1.3 Flight path

The length of the flight path is determined by a trade-off between obtaining a good energy resolution and a good efficiency. As the flight path is increased,

1. the time spread of neutrons of differing energies increases linearly, but the time resolution remains constant. So the energy resolution improves with increasing flight path, but it will reach a limit. This limit is determined by factors independent of the path length, such as the energy resolution of the proton beam.

2. the efficiency of the system decreases since the detectors will cover a smaller solid angle (the solid angle decreases as the square of the flight path length).

3. the absorption of neutrons increases as the neutrons need to traverse a longer distance through air between the target and the detector, also decreasing the efficiency.

The longest flight path available in the park is 200 m. The neutron detectors were positioned at a distance of 174.8 m from the target.

The coaxial cables from the hut to the dataroom were placed along the surface of the ground, and so the pulse propagation velocities may be affected by the diurnal temperature variations. Changes that would occur in the transit time are significant for the timing pulses, which are measured relative to a fixed point in the cyclotron radio frequency (RF) phase. The diurnal variation in propagation time was of the

order of 1 ns. This effect was minimized by splitting the experimental session into runs of about four hours each, so time variations within a run were well below the cyclotron pulse time uncertainty of about 1 ns.

The neutron flux was attenuated between the target and the detector. This reduced the intensity of the beam at the detectors, and thus the efficiency of the spectrometer. The following substances lie in the path between the target and the detector:

- a steel plate, of 1.2 cm thickness, at the end of the proton beam line to maintain the machine vacuum,
- about 174 metres of air, mainly O_2 and N_2,
- a 3 mm plateglass window of the detector hut.
- the 2 mm thick wall of the Al box which housed the detectors.

The neutron transmission is defined as the fraction of neutrons that actually reach the detector compared to all the neutrons emerging from the target towards the detector . The transmissions were calculated by Newman [NEW 91] for various energies. For energies used in this analysis they are 0.56±0.05, 0.62±0.09 and 0.71±0.14 at 120 MeV, 160 MeV and 200 MeV respectively.

3.1.4 Pulse selector

A difficulty experienced in the data acquisition are the *wrap-around* neutrons. These are the slower neutrons from a beam pulse on the target which are being overtaken by the faster neutrons from the next pulse. In section 4.4.1 a method for removing the wrap-around neutrons from the neutron spectra is discussed. It is desirable to have as large a pulse separation as possible to reduce this wrap-around effect. The pulse separation can be increased by using the pulse selector in which the selection ratio can be set from 1 in 2 pulses to 1 in 7 [NAC 87]. In these experimental sessions the selections of 1 in 6 and 1 in 7 were used. Table 3.2 shows the time spacing of the proton pulses at the various energies when using the pulse selector.

Table 3.2: *The period between proton pulses shown with and without pulse selection.*

Energy (MeV)	*RF (MHz)*	*period (ns)*	*pulse selection*	*PS period (ns)*
120	21.2	47.1	1:6	282.5
160	23.9	41.9	1:6	251.4
200	26.0	38.5	1:7	269.2

The pulse selector provides a sinusoidal signal at the same frequency at which the proton bunches arrive at the target, called the pulse selected radio frequency

(PSRF) signal. The arrival time of the neutrons at the detectors is measured relative to this PSRF (section 3.3.2).

At the Indiana University Cyclotron Facility a better method was used. There a stripper loop has been utilised which provided a pulse separation of 1.8 μs [FRI 85]. This enabled measurements up to excitation energies of 120 MeV at E_p=160 MeV, whereas at that proton energy we were only able to measure up to E_x ~45 MeV.

3.1.5 Beam swinger

The beam swinger was used to obtain neutron measurements at various angles with respect to the proton beam by varying the angle of incidence instead of the angle of observation. The available range is from −5° to 35°. The hut can be positioned along the flight path at an angle of 0°, 30°, 60° or 90° relative to the undeflected proton beam, so the possible angles of observation range from −5° to 125°. For the present data only measurements at 0°, 2° and 4° were taken. The beam swinger consists of three large dipole magnets [NAC 90]:

Magnet 1 is a circular pole deflecting magnet. It is used to set the angle at which the proton beam will hit the target.

Magnet 2 is a specially-contoured wedge-magnet used to guide the beam onto the fixed target. Using an excitation current of 190 A for this magnet a field of 1.35 T was obtained.

Magnet 3 is a deflecting magnet to guide the non-interacting beam and all charged reaction products into the beam dump. The value at which this magnet is set is not too critical, since the dump is about 30 cm wide.

The beam swinger has thus far been operated fairly reliably. However, the measured angular distributions at 200 MeV from the week-end of 21-24/06/1991 did not follow the expected angular trend. It was deduced that the angle settings were slighty incorrect for this data set (see section 5.1.1 for more detail).

3.2 Overall energy resolution

The energy of charged particles can be measured accurately by detecting the light output from the ionization they cause in a scintillating medium. They can also be measured by a magnetic spectrograph or a solid state detector, but for the uncharged neutrons all these tools are inapplicable [GOO 80]. A neutron can only be detected in a scintillator when it scatters off a charged particle which in turn causes ionization. The energy spectrum of that detected particle, resulting from a monoenergetic neutron source, is not monoenergetic, but has a continuous energy distribution [FIR 79, BRE 87]. This occurs because the neutron can scatter from different types of particles in the medium and the angles of the knocked on charged particle can differ. So the measured pulse height is not uniquely related to the neutron energy.

A better method for obtaining neutron energies is the time-of-flight technique, whereby the time the neutrons take to fly along a known path length is measured. In 1938 the initial proposal of using neutron time-of-flight spectroscopy was made by Alvarez [ALV 38, ALV 87]. The method was extensively used in experiments at low energy with reactions from light charged particles and photons from a range of accelerators [FIR 79]. Several nuclear physics research centres, for example NAC, IUCF, LAMPF, and TRIUMPF, have utilised time-of-flight for the (p,n) reaction [ZAF 80] in the intermediate energy range, obtaining time resolutions of about 1 ns or better in the intermediate energy range.

By using relativistic kinematics, the energy of the neutron can be calculated from the time-of-flight, and hence the energy to which the residual nucleus is excited. So the energy resolution of our system will depend mainly on the numerous timing uncertainties. In this section the various uncertainties which contribute to the overall energy resolution will be discussed.

3.2.1 Timing uncertainties

An overview of numerous timing contributions in a NTOF spectrometer is given by D'Agostini, *et al.* [DAG 81]. The main timing contributions arise from the spread of arrival times of protons in a beam pulse on the target, called the beam time width, and the intrinsic time resolution of the detectors.

Beam time width

The proton beam time width was often the largest contribution to the overall time resolution. The beam time was measured with a proton telescope continuously during the runs to measure the time quality of the beam as well as to check for drifts in the beam time.

The proton telescope consisting of a thin (5 mm) ΔE and a thick (50 mm) E scintillator (both made of NE102A), and was positioned at 30° with respect to the undeflected proton beam at about 1 m from the target. Both scintillators were coupled to R329, 2″ Hamamatsu Photomultipliers (with E931 bases). The proton telescope was set to detect elastic scatters from the (p,p') reaction. For elastic scatters the time structure of the proton pulses at 30° should be the same as the time structure of the beam pulses. This reaction was selected by gating only for the highest energy protons scattered in the direction of the telescope.

First a threshold was set on the E detector, which measured the full energy of the scattered proton, to select only the highest energy protons. Then these protons, which leave a characteristic amount of energy in the ΔE detector, were selected accurately by setting a tight energy window on the ΔE pulses. Finally the discriminated ΔE and E signals were put in coincidence to exclude any events that did not originate from the target. This ΔE/E coincidence was used to start a TAC and the PSRF (provided by the pulse selector) was used to stop it. The amplitude of the TAC pulse was then a measure of the time between the protons being injected into the cyclotron and arriving at the telescope (plus an arbitrary constant). The

FWHM of the distribution of the TAC output pulses provided the width of the proton beam pulses.

At the energies of 160 and 200 MeV it was noticed that the highest energy, elastically scattered protons were not stopped in the E detector. Thus they did not deposit their full energy and became indistinguishable from the lower energy, inelastically scattered protons. Therefore a 3 cm brass energy degrader was placed between the ΔE and the E detector, reducing the energy of the protons to about 120 MeV. They then stopped in the E detector and the procedure outlined above could be followed.

The finite measured time width of the beam is mainly due to the different path lengths which the protons of differing energies follow through the cyclotron. We also measured the drifts of the beam time relative to the PSRF reference signal. Goodman reported [GOO 79] that very small drifts in the magnetic fields in the cyclotron cause changes in the overall transit time of the accelerating particles in the cyclotron; the result is a time shift of the beam time. If the drift was significant over time, then in the off-line analysis long runs were split and the sections shifted relative to one another and added to reduce this effect.

The time resolution of the telescope itself was found by starting the TAC on the ΔE pulse and stopping it on the E pulse, using only elastic scatters. At beam energies of 120 and 160 MeV the FWHM of the peak was measured as 250 and 380 ps respectively. This accuracy was good enough to measure a beam timing width of about 1 ns.

For most of the sessions the beam time was about 0.7 ns. During some runs the time width degraded to ~1.5 ns, while for some runs it was improved to 0.4 ns.

Intrinsic detector resolution

During the (p,n) data acquisition background cosmic muons were detected. Those muons which deposited energy in each of the 6 detectors, and had thus traversed the whole vertical stack, were recorded.

The procedure for calculating the intrinsic resolution is described in detail in section 4.3.2. The average intrinsic resolution (FWHM) was found be 330±30 ps (similar for all detectors). For a specific experimental session it remained fairly constant; in between sessions changes occurred presumably because of changes in the quality of optical contacts between the scintillator, the light guides and the PMT's.

3.2.2 Energy uncertainties

There is a spread in the energy of the proton beam from the cyclotron, which can be tuned by adjusting the width of collimator slits at a bending magnet close to the exit of the cyclotron. During the (p,n) experiments the slits were set to give an energy resolution, ΔE_p(beam), of 0.075% [CON 92]. In Table 3.3 the proton energy uncertainty are shown for the energies used in the experiment. At each bending magnet along the beam line after extraction from the cyclotron the protons

Table 3.3: *Proton energy spread from the beam extracted out of the cyclotron and from the proton interacting at different depths in the ^{90}Zr, 134 $mg.cm^{-2}$ target.*

E_p (MeV)	ΔE_p(beam) (keV)	ΔE_p(target) (keV)
120	90.0	540
160	120.0	442
200	150.0	385

of differing energies will follow slightly different paths, which results in further time spreading of the proton pulse. So the actual contribution of ΔE_p(beam) to the overall time uncertainty (as shown in table 3.4) would be slightly more significant.

Another uncertainty in the energy of the proton arises from the uncertainty of the depth in the target at which the proton interacts. The incident proton looses energy by ionization in the target, so the further the proton traverses the target before the interaction takes place, the lower the proton energy. The maximum energy loss, ΔE_p(target), is between those protons scattering at the front and those scattering at the back of the target, up to 540 keV at E_p=120 MeV (table 3.3). This spread in proton energies results in a spread of neutron energies, which produces a spread in the flight time of around 800 ps at E_p=120 MeV.

3.2.3 Geometric uncertainty

The geometrical uncertainty arises from two contributions to the uncertainty in the flight path, L: firstly the overall uncertainty in the *surveyed distance* between target and detector, and secondly the uncertainty in the *interaction position* of the neutron into the detector, which changes from event to event.

The flight path uncertainty from the surveyed length of the path is 0.05 m. The uncertainty on the interaction position is 0.1 m, since the neutrons can interact at *any* position into the 10 cm depth of the detector.

So the flight path would only be known to 0.10 m accuracy. But the uncertainty of the depth of interaction can, however, be reduced to ~0.03 m by positioning the detector stack longitudinally to the beam. Then the time difference between the times of the two TDC's on either end of a detector can be used to determine the position of interaction to an accuracy of ~0.03 m.

The combination of the flight path uncertainty, and the uncertainty of the area of the detectors, provides the uncertainty in the solid angle subtended by the detectors. This error will be introduced when calculating the differential cross-section (section 5.1). The physical dimensions of the scintillator can be measured to an accuracy of 0.001 m, but the area for efficiently detecting neutrons is not so clearly defined. The neutrons interacting on the edges of the detector are likely to deposit only a small amount of energy in the detector without crossing the energy threshold. So an uncertain detection region of 0.005 m width around the edges of the detector

exists.

3.2.4 Total resolution

The various uncertainties can be combined to obtain an estimate of the overall time uncertainty, and hence the total energy resolution [MAD 83]. Two uncertainties, namely those in the position of the interaction in the target and in the detector, were rectangular distributions, while the others were gaussian distributions. These two uncertainties were divided by $\sqrt{12}$ before combining them in quadrature with the other uncertainties to obtain the total resolution [MAD 83]. Table 3.4 provides an overview of each of the uncertainties for the runs at E_p=120 MeV, $\theta = 0°$, and a flight path of 174.8 m, resulting in a flight time of ~1320 ns for the highest energy neutrons.

Table 3.4: *Combination of typical uncertainties for E_p=120 MeV, $\theta = 0°$ showing the total calculated energy resolution. During some runs a better beam time of up to 400 ps was obtained compared to the tabulated value of 900 ns.*

Type of uncertainty		*ΔEnergy (keV)*	*Δtime (ps)*
Time	beam time		900
	intrinsic detec. res.		330
Energy	ΔE_p(beam)	90	469
	ΔE_p(target)	540	811
Geometric	Detection position		218
TOTAL	time uncertainty		1358
	energy resolution	276	

The total time uncertainty is 1.36 ns, which would correspond to an energy resolution of 276 keV. The experimental energy resolution, obtained from the width of the IAS, is 575 keV. The expected uncertainty is about twice as good as the resolution obtained from the measured widths. Possibly the error on some of the quantities was underestimated, or there could have been time drifts in the stability of the proton beam which would have reduced the resolution. Note that not all of the errors above are totally independent. There is a partial correlation between the beam time and the spread in the beam energy [MAD 83].

Our total resolution is slightly better than the ΔE=660 keV obtained by Bainum et al. [BAI 80] for their (p,n) experiments on ^{90}Zr at E_p=120 MeV, L=62 m. Our best resolution was obtained at E_p=160 MeV, namely a resolution of 550 keV. This enabled us to observe more structure in the GTGR than had previously been seen at E_p=160 MeV, L=45 m, with a resolution of 1300 keV [TAD 86].

3.3 Determining and recording valid events

Two types of events, called *valid events*, were recorded by the neutron detectors in the hut:

neutron events occurred when a high energy pulse was detected in at least *one* of the six detectors. The fanned-in amplitude of the pulses from the phototubes at both ends of the detector had to exceed a neutron energy threshold (E_n^{thr}) to produce a neutron trigger. This energy threshold was the best compromise between a high E_n^{thr} that reduces the wrap-around neutrons, and a low E_n^{thr} that results in better count rates. The E_n^{thr} was set between 40 and 60 MeVee [NEW 91].

cosmic-6 events were recorded when a pulse was detected in each of the 6 detectors. The cosmic muon threshold was set at a value above the noise, but well below the cosmic peak, which corresponded to an average energy of 22.3 MeVee being deposited in a detector. The cosmic-6 rate was fairly low at about 0.5 events/sec.

For each of these events the following was recorded: the arrival time and amplitude of the pulse in each of the detectors and a number which indicated in which of the detectors the event(s) took place. Other recorded data are the $\Delta E/E$ pulses and the scalar to measure the integrated current.

3.3.1 Layout of recording apparatus

The main section of the electronic equipment was situated in the hut housing the neutron detectors in the park. This included the circuitry (using NIM modules) to record time and amplitude signals of the neutron detectors with a CAMAC crate (the schematic layout is shown in figure 3.3 and will be explained below). The electronics for obtaining the ΔE and the E pulses from the proton telescope (details in section 3.2.1) was inside the main hall near the beam swinger vault. In the dataroom was the beam time ADC, the dead time correction circuitry, the current integrator connected to the Faraday cup in the beam dump, two CAMAC crates, the micro-programmable Branch Driver (MBD) and the VAX computer. The computer control and spectra display of the experiment could be done either in the dataroom or in the hut.

The three CAMAC crates, one in the hut and the other two in the dataroom, were used to read the experimental data from the CAMAC modules. A micro-programmable Branch Driver (MBD-11) acted as an interface between the CAMAC crates and the VAX 11/730 acquisition computer. The data was recorded on magnetic tapes and replayed offline on the VAX 6000-330 at the University of Cape Town.

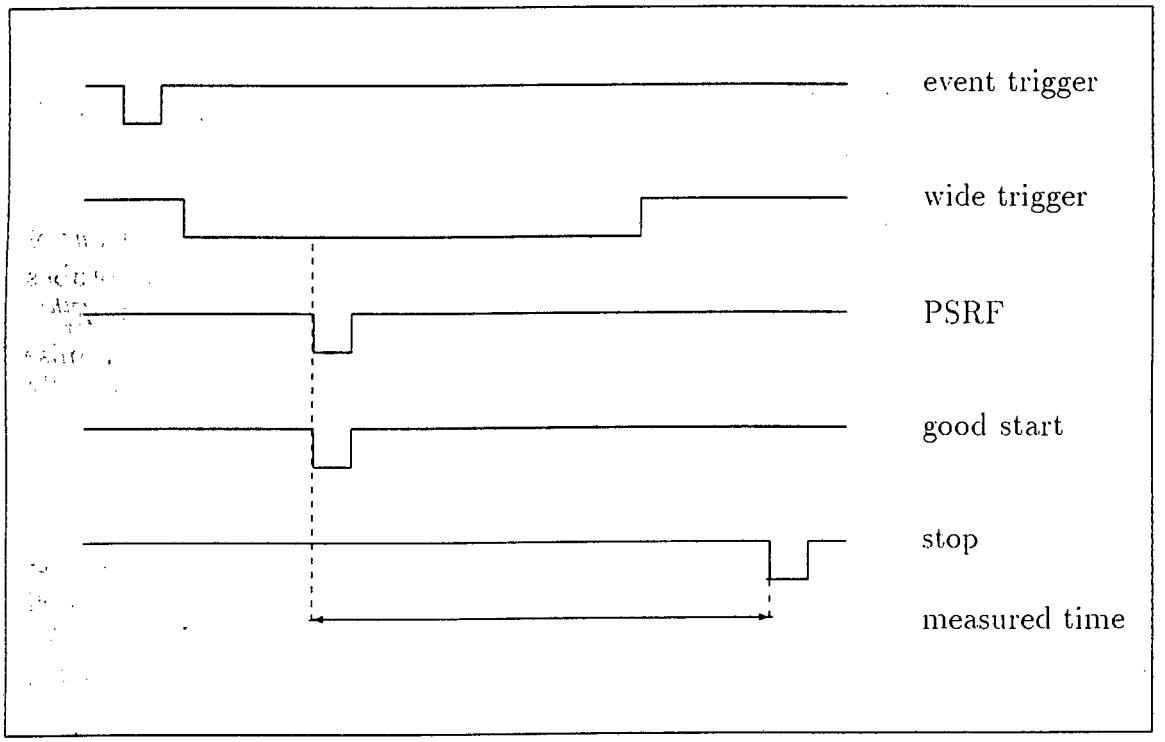

Figure 3.2: *Timing measurements of valid events, using the PSRF as a start, and a delayed event pulse as the stop. See text for explanation.*

3.3.2 The method of timing measurements

A neutron emerging from the target in the (p, n) reaction cannot be used to produce a start pulse. It is uncharged, which means it is not ionizing, and can thus not be detected twice along its flight path [GOO 84]. However, the cyclotron pulses are tightly bunched (within about 700 ps, as shown in section 3.2.1), so the *start* time could be taken from the cyclotron RF accelerating voltage. The pulse selector was utilised (section 3.1.4), so actually the PSRF signal was used for the start. The *stop* time was then formed by the signal from the detected neutron event. The cosmic-6 events are unrelated in time to the PSRF, but for recording purposes the same timing method as for the neutron events was used.

There are, however, many more PSRF start pulses than there are stop pulses from the events. So the neutron event trigger (which will be explained in section 3.3.3 below) had to be combined with the PSRF to produce a good start only for valid events, and to produce only *one* good start per valid event.

The method of measuring the time as stated above will be illustrated using figure 3.2. The first pulse on the figure (from the top) is the *event trigger*. This is stretched to produce a *wide trigger* (next pulse). This wide trigger was just shorter than the pulse separation between successive *PSRF* signals (next pulse shown), which was about 260 ns (as listed in table 3.2). Hence there would be only *one* PSRF signal for each valid event.

The wide trigger and the PSRF were placed in coincidence, producing a *good start* (as on the figure). Note that the time of this good start is determined by the

PSRF, ie. by the beam, in this coincidence. Sometimes the time of the coincidence was set by the wide trigger, resulting in spurious events as described in section 3.3.4. Part of the original signal from the detector had been delayed by about 320 ns such that it will be later than the last possible start pulse. It should be noted that this is the *same* signal from which the trigger had been formed, only with a difference in delay. It is then used as the *stop* shown on the figure, and the measured time is indicated by the arrow.

3.3.3 Electronic event triggering

The method of triggering for valid events using fast electronics will now be described. The outline of the circuitry in figure 3.3 is simplified to show the modules for only one detector. Each detector has two photomultiplier tubes, with their own high voltage supplies, connected to it. Two anode signals from each PMT are used: part of the signals were delayed, the other part was used to determine if the event was of interest to us (ie. a *valid* event). If so, then the delayed signals were used to record the amplitude and time of the event pulse.

The one anode pulse was attenuated and delayed by about 320 ns until an event trigger could be generated. A valid event would open the ADC gate, and the amplitude of the pulse would be measured by the ADC.

The other anode pulse was split in a 50Ω pulse splitter. One output of this splitter was sent to a constant fraction discriminator (CFD). One CFD output was delayed by ~300 ns, and would act as the TDC stop in the case of a valid event. Another CFD output was combined with the CFD output from the other PMT of the same detector in a mean timer module. From the mean timer an output was discriminated and recorded in the pattern register. This pattern register showed in which of the detectors the event took place, as well as what type of event occurred (each type of event sets a specific bit). Another mean timer output was set in coincidence with pulses from the other five detectors, thus determining a cosmic-6 event. The procedure for setting the coincidence was done using three 4–fold coincidence units: two to determine time coincidence between the top three or the bottom three detectors, and the third to determine coincidence between both these sets of three detectors. One output set the pattern register as the cosmic-6 bit, while another was sent as a valid *cosmic-6 event trigger*.

The other output from the splitter (for *both* PMT's of one detector) were summed in a quad linear gate and sent to a 6–channel discriminator with similar signals from the other five detectors. In this unit the neutron thresholds for each of the detectors was set, such that only neutrons depositing above about 40 MeVee in a detector were recorded. The 6 discriminated signals were OR'ed to form a *neutron event trigger*, which also set the neutron bit in the pattern register.

The two types of event triggers, cosmic-6 and neutron events, were OR'ed in a four-fold coincidence unit, set at coincidence level one. If the event trigger module was busy, further events were vetoed. Then the trigger of a valid event was stretched to form the *wide trigger*, which was set in coincidence with the PSRF signal as explained above.

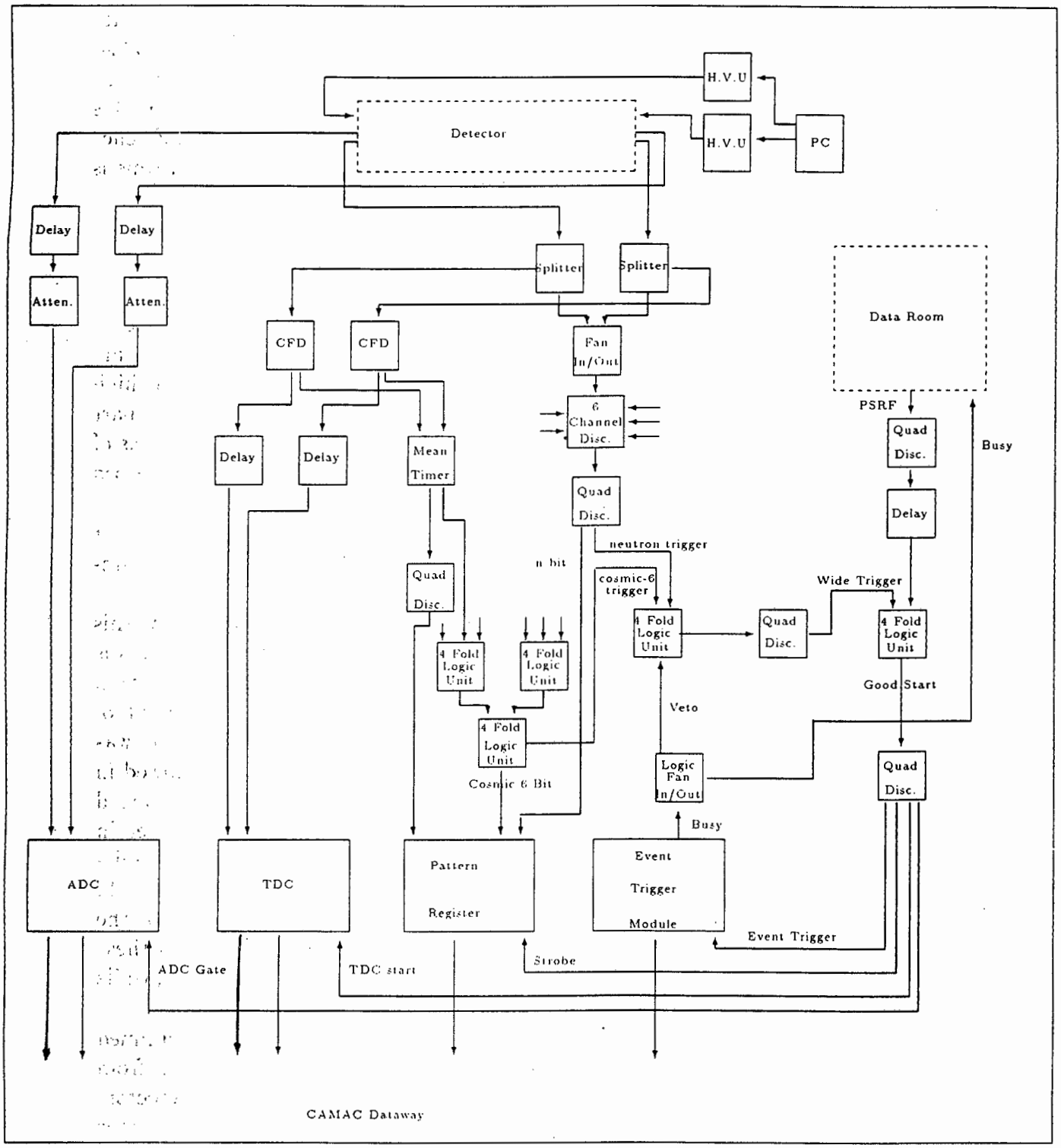

Figure 3.3: *Electronic layout for one of the neutron detectors in the hut [NEW 91].*

The coincidence output, called a *good start*, is fanned out through a quad discriminator into four pulses with the following functions: the event trigger, the strobe for the pattern register, the start for the TDC's and the gate for the ADC. As mentioned above, one anode pulse had been delayed so that it could be read into the ADC once a valid event had been determined, and the one output from the CFD was delayed such that it would form the stop of the TDC's in the case of a valid event.

3.3.4 Spurious spike due to electronics

At the end of the mean time spectra a sharp peak can be seen (channel 930 on figure 4.1). This is due to the electronics and is not a feature of the neutron energy.

As explained in section 3.3.3, the timing of an event begins with a *good start* and ends with the delayed signal of the event. In figure 3.4 it is shown that a *good start* is the coincidence between the *wide trigger* and the PSRF (shown as PSRF 1 on the figure). Usually the timing of this coincidence is determined by the PSRF. But *if* the

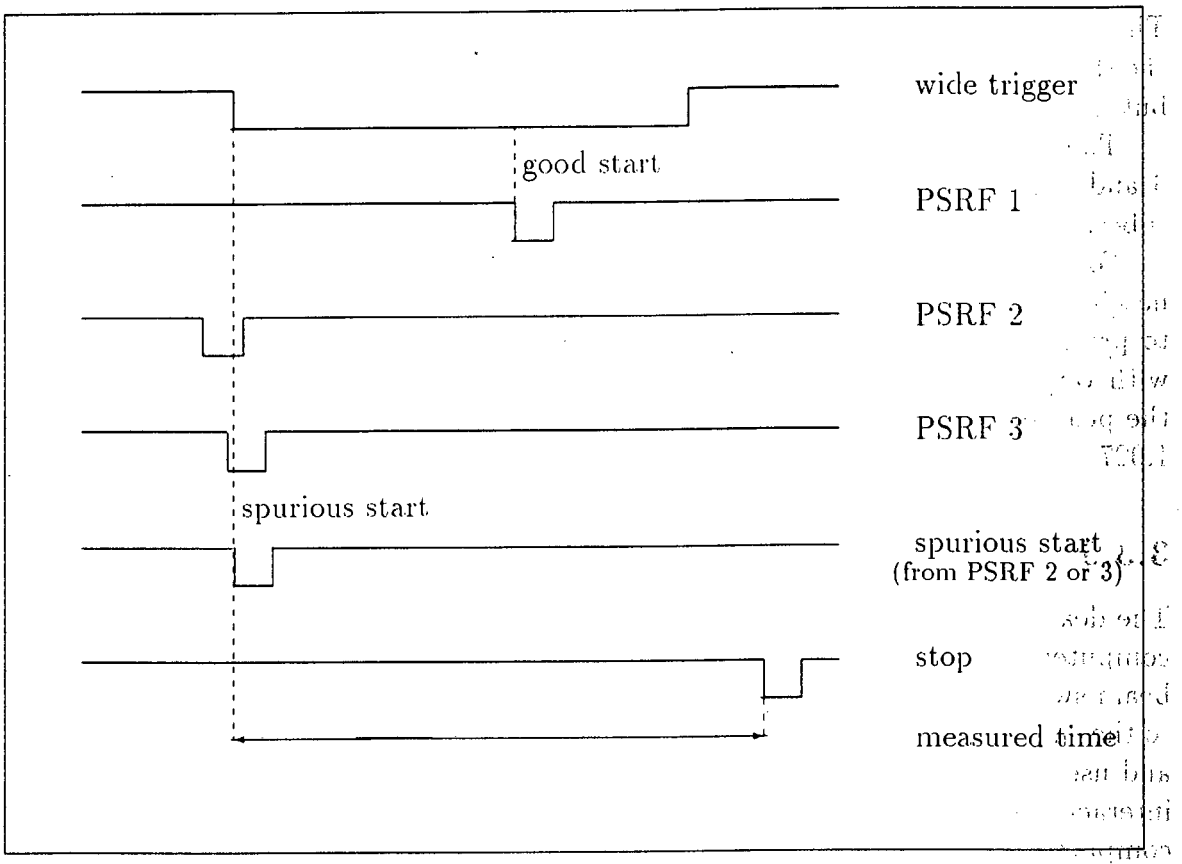

Figure 3.4: *For the longest possible time measured for an event, the* same *time is recorded for PSRF signals arriving just before the wide trigger (see text), resulting in a spurious spike in the mean time spectrum.*

PSRF comes slightly before the wide trigger (such as PSRF 2 or as PSRF 3), and the coincidence requirement is still met. *then* the start timing comes from the wide

trigger, which has the same timing structure as the stop. All such pulses, ranging within the width of the PSRF (ie. in the range of PSRF 2 and PSRF 3), will be recorded with the same time, forming the spurious spike. Hence the width of the PSRF should be as narrow as possible to reduce the number of these events.

These spurious events are recorded with the longest measurable time. So only neutrons which are almost wrapped around to the next beam pulse are affected, and thus the neutrons in the region of interest at earlier times are not influenced by this effect.

For cosmic-6 events the delay in the electronics is longer than for the neutron events (mainly due to the 3 logic units used in forming the cosmic-6 trigger). The maximum time that can be measured for them is shorter than for neutron events by about 21 ns. So the spurious spike for cosmic-6 events is formed 21 ns earlier. This spike is not visible in the neutron spectra, since all the cosmic-6 events were excluded when generating the spectra.

3.3.5 Electronic settings

The high voltage on each of the photomultiplier tubes was set manually to equalise the shapes and gains of pulse height spectra. The average voltage was about -1500 V, but individual values ranged from about -1400 to -1700 V.

The gains on the ADC pulses were adjusted such that the positions of the cosmic-6 and neutron peaks were at similar channels for each of the 12 photomultiplier tubes.

For each session of experiments, the TDC's were set to nominal values of 4 channels/ns. They were calibrated exactly such that the time spectra could be normalised to precisely 4 ch/ns during the off-line analysis. This was done by feeding a pulse with varying known delays into the TDC's and then noting the channel number of the peak in the time spectra. The relative calibration factors ranged from 0.990 to 1.027, depending of which TDC's were used.

3.3.6 Correction for electronic dead time

The dead time was corrected for by only recording the integrated current when the computer was not busy. The non-interacting protons were deflected by the third beam swinger magnet (behind the target) onto a Faraday cup which was connected to the current integrator unit. The signal of the current integrator was discriminated and used to measure the amount of charge passing through the target that did not interact. But the recorded current integrator signal was vetoed when the acquisition computer was busy, thus correcting for the dead time. The dead time usually varied between 2 and 5%.

3.3.7 Neutron detector efficiencies

The neutron detection efficiency in the neutron time-of-flight spectrometer was determined using the secondary-measurement method. Watson, *et al.*, [WAT 83] pro-

vide an overview of other available methods: the direct measurement technique, indirect methods and the computational method.

Two measurements are needed in the secondary-measurement technique. In our case the yield measured by our detectors for the $^{7}Li(p,n)$ reaction, of which the neutron cross-section is known, was compared to the measured yield of the $^{90}Zr(p,n)$ reaction, for which the cross-section is unknown. Since the yields are proportional to the cross-section and the neutron detection efficiency, and the proportionality constants could be measured, our detector efficiencies and the known cross-sections could then be calculated.

In our experiment the laboratory differential cross-section for $^{7}Li(p,n)^{7}Be(g.s.+0.43\ MeV)$ as reference cross-section was useful. This is because 0° differential cross-sections for transitions to the ground and first excited state (at E_x=0.43 MeV) in ^{7}Be at a number of beam energies are available in the literature [TAD 87, WAT 89], and the reaction has a high cross-section. So, during our (p,n) experiments only short runs on ^{7}Li of 10 min were sufficient in between the longer runs of ~4 hours on other targets. Thus the efficiency determination became an integral part of the acquired data.

A collaborator, R.Newman [NEW 91], determined the experimental efficiencies. For extracting differential cross-sections for summed runs, the weighted efficiencies for all six detectors and for all runs were obtained. For ^{90}Zr at E_p=200 MeV the weighted efficiencies are 2.11% for the summed 0° spectra.

In the following chapter the analysis performed on the cosmic-6 and on the neutron events, acquired at NAC in the procedure outlined above, will be described.

Chapter 4

Analysis of the events

This chapter begins by defining the features in the neutron spectra that will be used in later on. Then follows the discussion of two applications of the cosmic-6 events. For the neutron events it is then explained how the problematic wrap-around events were accounted for, and which events were rejected in generating the mean time spectra. Finally an outline of the peak-fitting procedure used to extract the number of events for peaks corresponding to specific transitions will be given.

4.1 Description of spectra

A typical *mean time spectrum* can be seen in figure 4.1. The mean time (of both TDC times of one detector) will provide the TOF independently of the impact position along the detector. This occurs since the mean photon transit time from the scintillation event to both ends of a long detector is independent of the position of interaction [MAD 83, BRE 87]. Hence in the analysis mean time spectra were generated for each of the six detectors by averaging the time of both TDC's for a detector. The mean time spectra show, from left to right, increasing time-of-flight of the neutrons. This increasing neutron flight time corresponds to a decreasing neutron energy (in a non-linear manner), and hence an increasing excitation energy of the daughter nucleus. The main features in these spectra, as labelled in figure 4.1, will now be described briefly:

- the **wrap-around region** consists of slow neutrons from a previous beam pulse; it can be seen from channel 0 to about 200, but is hidden underneath the rest of the spectrum,
- a number of **discrete states**, whose intrinsic width would be less than the instrumental resolution of ~570 keV,
- a few **broad peaks**: the Gamow-Teller giant resonance (at channel 350), which is a combination of many close unresolved discrete states, and a dipole resonance (at channel 500),
- a featureless **continuum** in high excitation energies (above channel 500), slowly decreasing with increasing excitation energy,

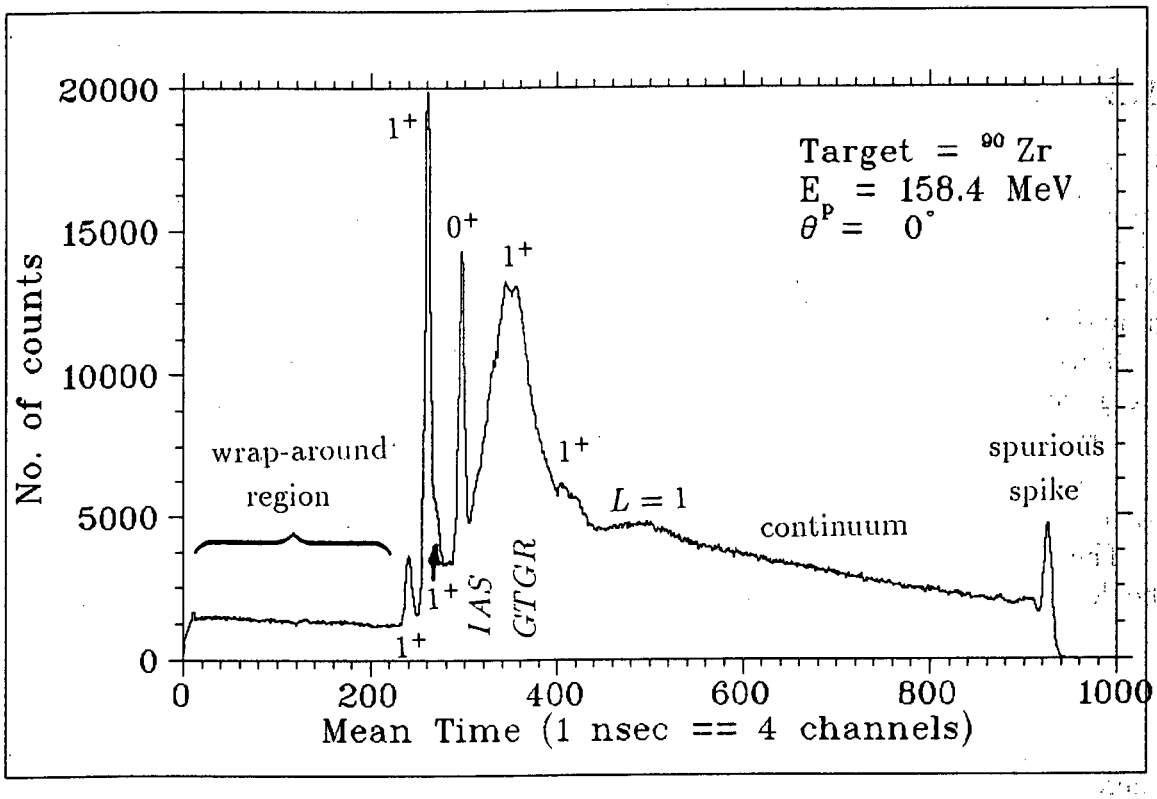

Figure 4.1: *A typical mean time spectrum showing the main features for the* ^{90}Zr *target. This spectrum was generated from 9 hours of beam time, with an integrated charge of 15 mC and a target thickness of 134 mg.cm*$^{-2}$.

- a **sharp spike** at the end of the spectrum (channel 930) due to the instrumental effect explained in section 3.3.4,
- **overflow events** in the last bin of the spectrum (channel 2048, usually not plotted on the scale of interest) in one detector, caused by events in another detector which produces a common TDC start, but for which this detector does not generate a TDC stop signal.

The two types of events, the *cosmic-6 events* and the *neutron events* were used in the analysis. The spectra at zero degrees were used, because they correspond to almost zero momentum transfer, in which case the results can be compared to β-decay. The goal is to extract differential neutron cross-sections, to calculate the sum of all the Gamow-Teller strengths and to compare this to the theoretical Ikeda sum rule.

4.2 Excitation energy spectra

From the time of arrival of the neutrons at the detector the energy of the neutrons can calculated. The energy of neutrons from a specific transition need to be known. Then the spectra can be plotted in terms of the energy to which the nucleus becomes excited by the (p,n) reaction. The energy of the neutrons from the transition to the ground state was calculated using relativistic kinematics.

Since the arrival times are measured with an arbitrary additive constant, the energy of neutrons in at least *one* peak in the spectrum must be known. In the ^{90}Nb spectrum the IAS at $E_x = 5.14$ MeV is a well-known, clear peak. Its position in the time spectrum was used to calculate the corresponding excitation energies for the other neutrons.

The time the neutrons from the transition to the IAS state would take to fly to the detectors was calculated by

$$t_n/L = 3.336404 \left(1 - \left(\frac{939.553}{T_n + 939.553}\right)^2\right)^{-1/2} \text{[ns/m]} \qquad (4.1)$$

where L=174.6 m is the path length between the target and the detector and T_n the kinetic energy of the neutrons from the transition to the IAS.

4.3 The cosmic-6 events

Cosmic muons provide a continuous background of events. Some of the muons interacted in only one or a few of the detectors, while others interacted in all six of them. In section 3.3 it was explained how the criterion was set up for recording cosmics which interacted in all six detectors. Here an overview of two uses of recording these cosmic-6 events will be given:

1. determining of the intrinsic resolution of the detectors,
2. obtaining an estimate of the neutron threshold for each of the six detectors.

Another use of the cosmic-6 events could be to monitor the stability and performance of the detectors.

4.3.1 Event rejection

Some of the events taken by the cosmic-6 trigger had to be rejected. A cosmic-6 event, requires a trigger in all 6 detectors, but for some events (of the order of 10%) the time recorded for some TDC's was either zero or overflowed.

Due to cable and electronic delays, there are different time delays for the times of each of the TDC's. During data acquisition at NAC the times of the cosmics have to lie within the wide trigger (as described in section 3.3). If the time is so early that at least one TDC is recorded per detector, the event fulfills the cosmic-6 requirement, but some of the times of the other TDC's may be recorded as zero. These events were rejected, because not all the necessary information was recorded.

Overflow events occurred when a pulse was detected in one of the two TDC's, but not in the other. That TDC was then not stopped and thus overflowed. These events were also removed.

4.3.2 Intrinsic resolution calculations

The difference between the detection time of an event from either end of a detector provided a measure of the position along the detector where the event took place. Muon fluxes at sea level have a mean energy of 2 GeV, and so the muons travel at relativistic velocities in straight lines through the stack of six detectors. This path of the muon can be partially reconstructed by lining up the interaction position in all six detectors.

Unknown delays in the electronics and the cables for each detector shift the time differences of the detectors relative to one another. These delays are called the time offsets. However, these relative offsets can be found by taking a large number of cosmic-6 events from a run and varying the time offsets such that the reconstructed paths lie as close as possible to a straight line fitted through the time differences.

By then using the time difference and these time offsets for each of the detectors, the position, x, along the detector where the event took place can be determined using

$$x = \frac{1}{2}(t_R - t_L)v_{\text{eff}} + C_{\text{offset}} \tag{4.2}$$

where v_{eff} is the effective light velocity in the detector, and C_{offset} is the offset due to cable and electronic delays. The v_{eff} can be obtained by measuring the width of the time difference curves, which should be twice as large as the time the light takes to traverse the length of the detector, and then using the physical length of the detector to calculate the effective velocity of light in the detector. The effective light velocity was found to be $\sim$15 cm.ns^{-1} [KAB 90] in the neutron detectors.

The differences between the reconstructed paths and straight line fits to these points were called the residuals. A measure of the intrinsic detector resolution was then found by binning the residuals into histograms and calculating the full width

at half maximum (FWHM) of the distribution for each detector. This intrinsic resolution should remain stable over different runs if the apparatus is not altered. Figure 4.2 shows that the resolution stayed at about 330±30 ps for each of the detectors for a set of 52 runs.

4.3.3 Threshold determination

During the (p, n) experiments no high energy neutron sources are available to calibrate the amplitude spectra. Although the channel number of the neutron thresholds can clearly be seen in the amplitude spectra, the actual neutron energy of this threshold is not known. The neutron energy cannot be measured accurately by the pulse height of an event, because only the energy of the scattered charged particles is detected. A possible calibration source are the muons from cosmic rays. They traverse the detectors at energies of about 2 GeV, and are thus minimum ionising, and deposit 2.23 MeV/cm in the scintillator [NEW 91]. But the cosmic events traverse the detectors at different angles, and hence deposit differing amounts of energy in the detectors. If the traversing angle is measured relative to the vertical axis of the detectors, then vertical muons would interact at 0°, and muons traversing the 60 $cm \times 60$ cm stack from one corner to the opposite corner at about 45°.

The angle at which the muons traversed the detectors, θ_t, was calculated from the interaction position in each detector. The muon events were split into 5° bins according to their traversing angle. The position and amplitude of about 10000 events were plotted for each bin in figure 4.3 for one detector on the outside of the stack, detector 1 (the bottom detector), and one near the middle, detector 3.

It can be seen that the higher the angle, the greater the energy deposited in the detector. For each set of angles the energy deposited in the detector can be calculated by $E_\mu = 22.3/cos\theta_t$. The position of the maximum of the peak in each amplitude spectra was measured and plotted against energy deposited in the detector. By extrapolating a straight line through these points to the channel at which the neutron threshold lies, the energy of the neutron threshold was found to be 37 ± 5 MeVee at $E_p = 120$ MeV and $\sim 60 \pm 5$ MeVee at $E_p = 160$ MeV, assuming linearity of the scintillator response.

On the amplitude curve for detector 1 (figure 4.3), low amplitude shoulders can be seen on the left of the amplitude curves. These shoulders are due to cosmic muons which traverse only part of the thickness of the top and bottom detectors. For the inner detectors the muons *have* to traverse the whole thickness of the detector to fulfill the cosmic-6 requirement, while for the outer ones, the muons can enter (or leave) the stack through the sides of the detectors. The cosmic-6 thresholds are fairly low in *each* of the detectors, so muons that only traverse part of the outer detectors get detected, as long as they deposit more than the threshold energy.

On the graphs on the left of figure 4.3 the position of interaction for muons is shown for a range of interaction angles. For both detectors 1 and 3 the muons which interact vertically lie in a rectangular distribution along the whole length of the detector. As the angle of interaction increases, the position where the muons can interact in each detector becomes limited, as the muons still have to fulfill the

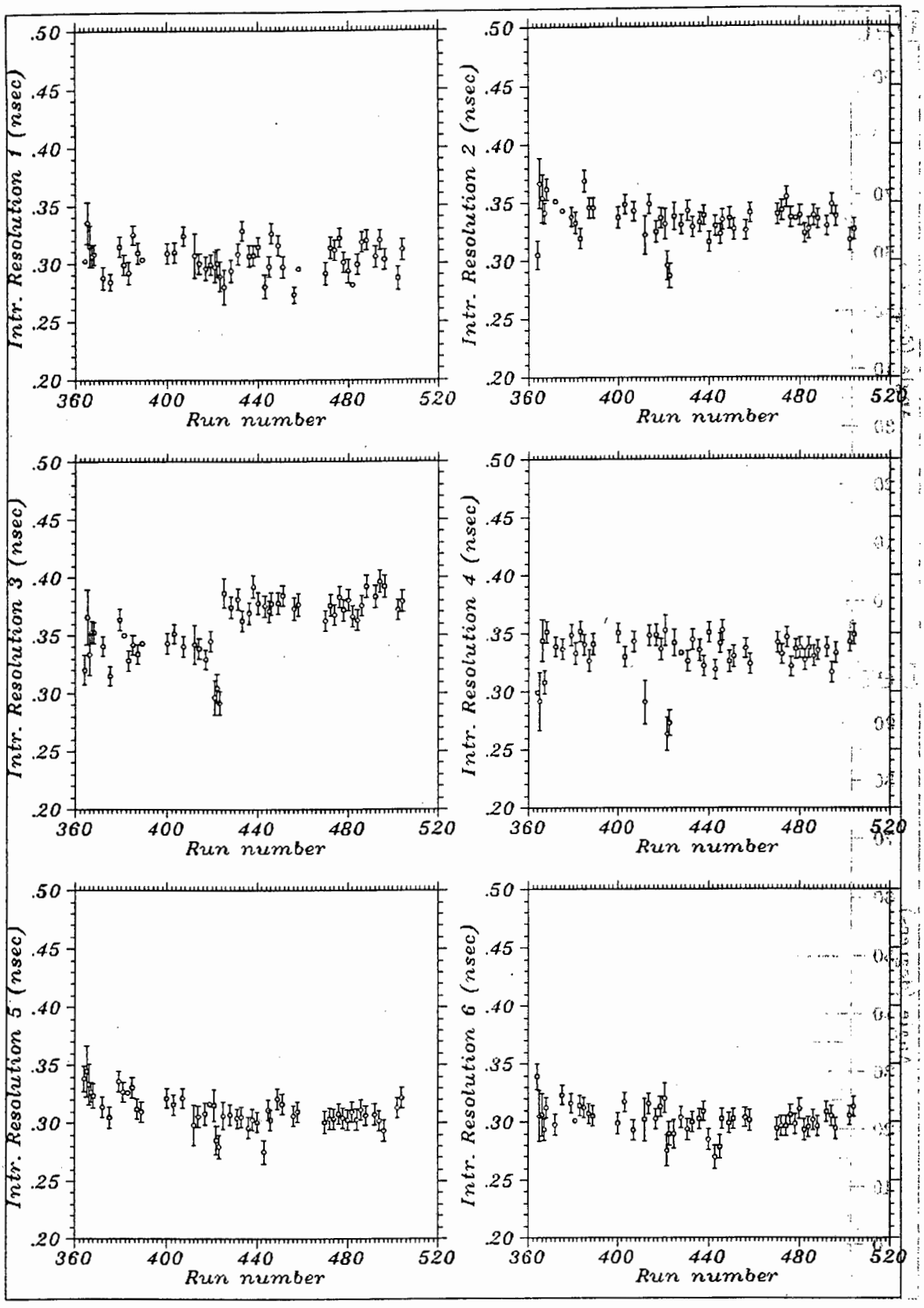

Figure 4.2: *Intrinsic resolutions for each of the six detectors, calculated using cosmic-6 events for a set of 52 runs.*

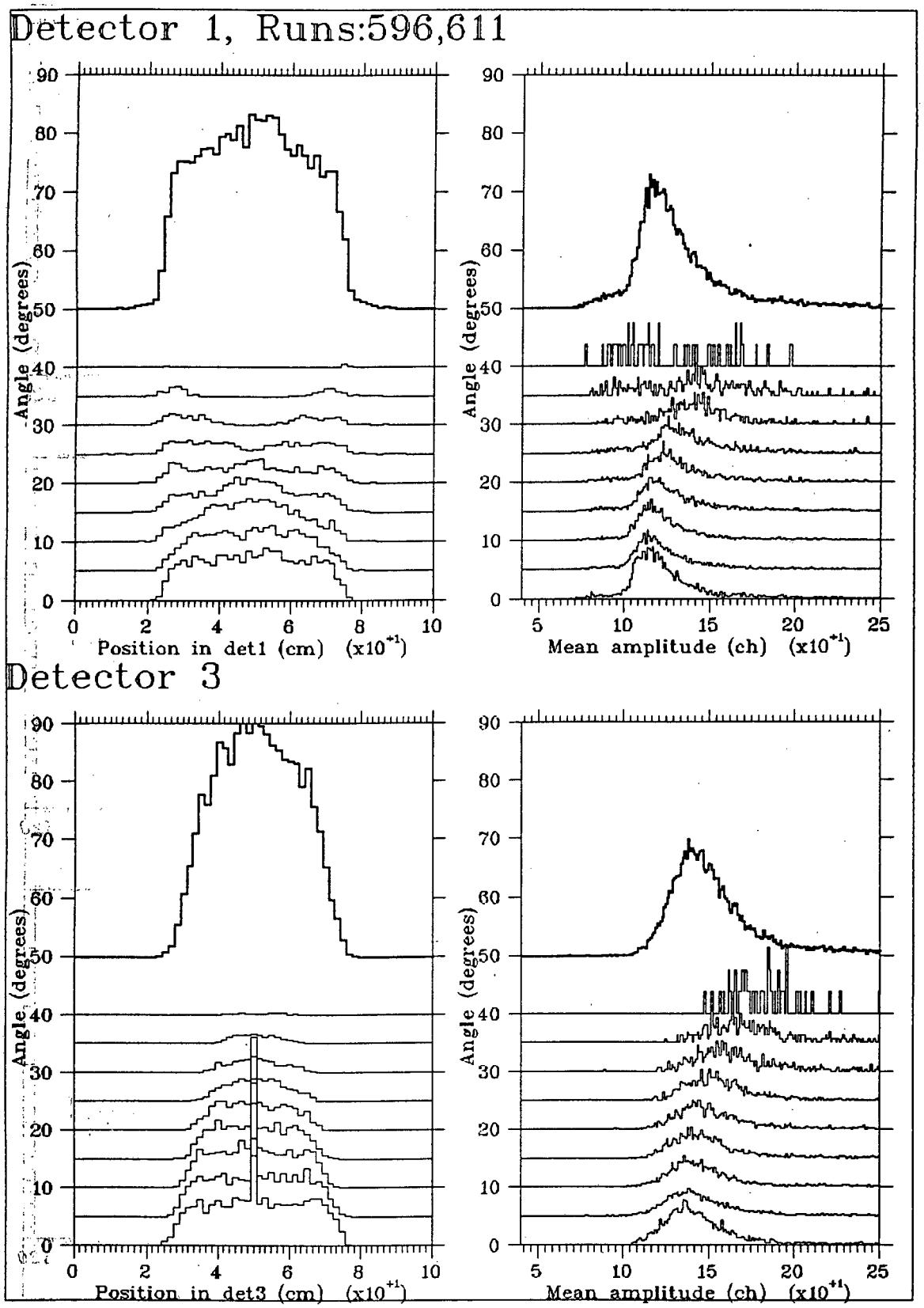

Figure 4.3: *Position along the detector and amplitude for cosmic-6 events at different angles through the detector stack. Each histogram represents a range of 5°; the bold curve is the sum of the others. Position curves are on the same vertical scale, whereas the amplitudes are on differing vertical scales so that the position of the peak can be seen more clearly.*

cosmic-6 requirement. Thus diagonal muons *have* to cut detector 1 on the ends of the scintillator, while they *have* to pass through detector 3 near the centre. The gradual change of the rectangular distribution to each of the two extremes can be seen clearly. The central spike in the position for detector 3 in channel 50 probably arises from events which had times close to zero, but were not removed when the zero events were disregarded.

4.4 The neutron events

The condition for an event to be recorded as a neutron event is that the amplitude signal for at least one detector is above the high neutron threshold. The amplitude signals for the two PMT's of each detector are summed using a linear fan-in module, and a single threshold is set for this combined pulse.

4.4.1 Wrap-around neutrons

The wrap-around neutrons are recorded when the slow neutrons of one pulse are overtaken by the fast neutrons of the next pulse. When these slow neutrons get detected, they will be recorded one beam period later than the faster neutrons. They will thus be overlaid on the spectrum of the faster neutrons. Since the spectrum at higher excitation energies is quite featureless, the wrap-around neutrons produce a fairly continuous 'background' in the spectrum. During some of the runs even double wrap-around occurred (ie. the neutrons were recorded two beam periods later).

For our long flight path of 176 m this makes an important contribution to the unwanted data. There are two ways to reduce the wrap-around in the experiment:

1. the beam pulse separation can be increased so that the lower energy neutrons can arrive at the detectors before the next fast ones arrive,

2. the neutron threshold can be increased so that the lower energy neutrons, which would appear a period later and which produce a smaller pulse height, are cut out.

Both these methods unfortunately also reduce the efficiencies. The pulse separation was set as large as possible (1 in 7) for 200 MeV (for lower energies the 1 in 5 or 1 in 6 selections were used). The neutron thresholds were set at the lower energy end of Landau distribution of the energy of the charged particle scattered by the neutron. This was done to include the neutron events, but to eliminate nearly all of the muon events from cosmic rays. If the neutron thresholds can be found accurately, then the amount of wrap-around can be determined more accurately. A method for determining this neutron threshold was described in section 4.3.3.

For example, by estimating $E_{th} \sim 60$ MeV at $E_p = 160$ MeV as shown above, the lowest energy neutrons to be measured would correspond to a nucleus excitation energy of $E_x = E_p - Q - E_{th} \sim 90$ MeV. In figure 4.4 it can be seen that this would be a double wrap-around. Note that the reduced width and increased amplitude

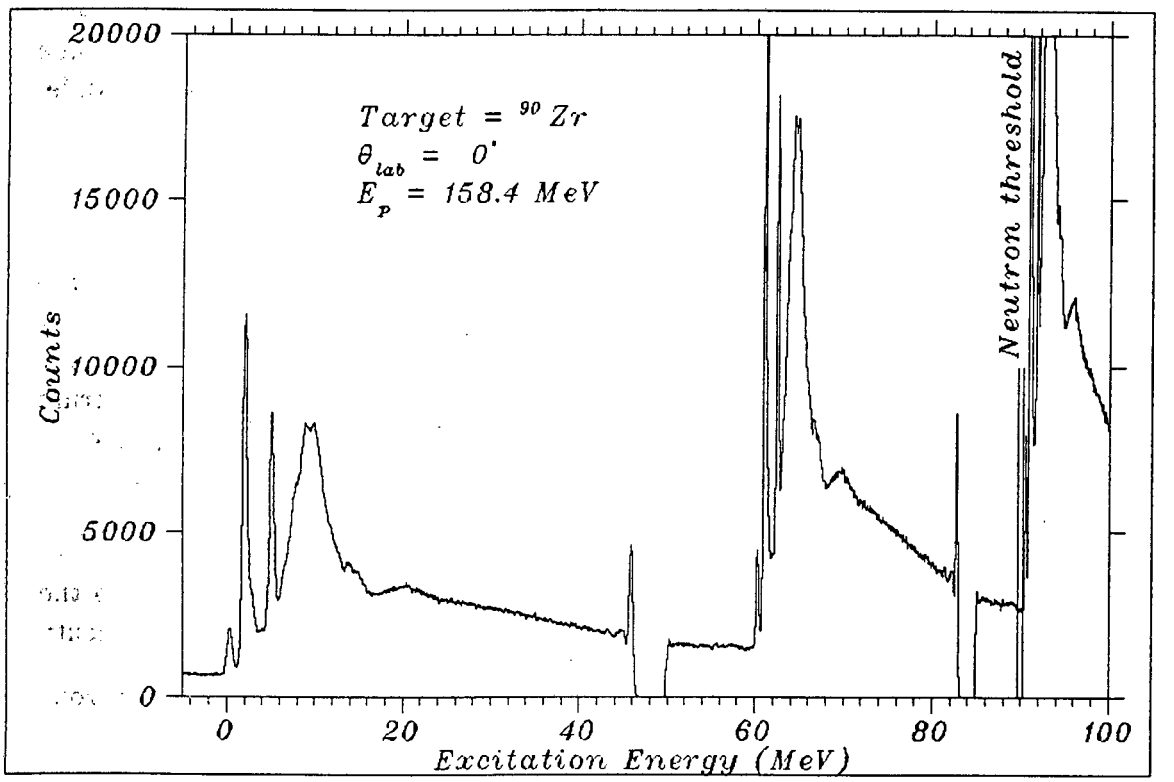

Figure 4.4: *Three beam periods showing the continuation of the wrap-around neutrons from one spectrum to the next. The pulse spacing is 251.4 ns, which is then also the time separation between the successive neutron spectra.*

of the 2^{nd} and 3^{rd} neutron spectra is the result of the non-linear conversion of the time to energy spectra. Of the 2^{nd} and 3^{rd} neutron spectra, only the neutrons in the wrap-around region correspond to the excitation energy on the axis scale, since these neutrons are actually recorded relative to the first pulse.

In the (p,n) reaction, the first neutrons to arrive at the detectors are those with the highest energy, and would be the neutron produced in the reaction from the target ground state to the daughter nucleus ground state. In ^{90}Zr the ground state has $J^{\pi}_{g.s.} = 0^+$, but the ^{90}Nb has $J^{\pi}_{g.s.} = 8^+$. The transition between ground states would be a large angular momentum transition (ie. L$\gg$0), which would peak at a high angle. At the small angles the simple F and GT transitions dominate, so the ground state peak is not seen in these low angle (p,n) spectra. In ^{90}Nb the first peak observed in the time spectrum (due to the neutrons of highest energy) is a 1^+ state corresponding to $E_x \sim 0.9$ MeV in figure 4.4. Thus any events in the time spectrum *before* this state must either be from different types of events (such as cosmic muons), or be neutrons wrapped around from the previous pulse.

If this early time region is entirely due to wrap-around, then it should match well onto the high excitation energy part of the spectrum. This was tested by shifting the spectrum by one beam period of 251.4 ns and fitting a decaying exponential to these two regions in the spectrum as in figure 4.5. The function should then actually continue from the wrap-around region up to the higher excitation energies and could then be subtracted to remove all the wrap-around. If the function still has a substantial magnitude at the high excitation energy end, it should even extend over to the next spectrum.

The exponential function was found to fit very well onto these two regions (see figure 4.5) . This would imply that the wrap-around has fallen off substantially after one beam period. Estimates of the neutron threshold show that the wrap-around should extend much further. It is thus suspected that the wrap-around drops off to zero somewhere before the threshold. Exactly how it falls off is not known, but this is the information that is needed to be able to extrapolate the function fitted to the wrap-around data underneath the rest of the data.

The crudest manner to eliminate the wrap-around is to extrapolate a straight line fit of the wrap-around region underneath the rest of the spectrum. On figure 4.5 it can be seen that for the earliest discrete peaks, which are of most interest in this analysis, the difference between subtracting a straight line fit or a decaying exponential is small. For analysis of the high excitation energy continuum, the shape of the wrap-around which is removed is very important. It would, however, be most advantageous to use hardware settings to reduce the wrap-around.

It was checked if the wrap-around neutrons could be removed by software amplitude cuts. The wrap-around neutrons have less energy than the neutrons in the initial spectrum. So they may deposit less energy in the detectors than the faster neutrons. The amplitude spectrum of the neutrons in the wrap-around region was compared to that for the rest of the spectrum. The amplitude spectra look very similar, the only difference being that the amplitude spectrum of the wrap-around neutrons has a slightly sharper peak. Hence an amplitude cut cannot be applied to remove these wrap-around events.

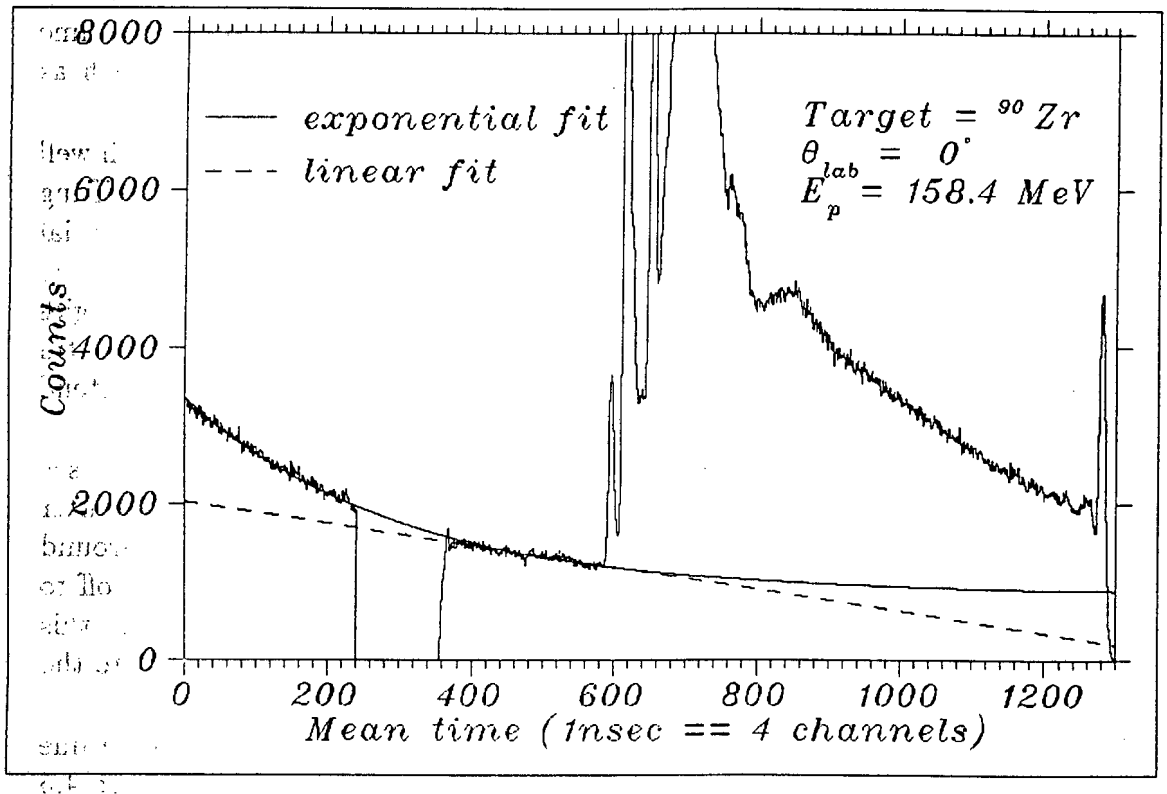

Figure 4.5: *Decaying exponential and straight line fit to the wrap-around region.*

4.4.2 Event rejection

A number of events were rejected before the mean time spectra were generated. A brief reasoning for the removal of each of these events will be given.

Cosmic-6 events

The cosmic-6 events are in no way related to the neutron events, thus were not included in the neutron time spectra. The cosmic-6 events would have no effect on the cross-sections of discrete states, because their arrival times form a continuous flat distribution. Nevertheless, they would just produce unnecessary background.

Single zero events

For some events the TDC digitization of the time of the signal from the PMT at one end of a detector provided a zero time measurement. It was suspected that this could be a hardware problem. This would imply that the mean time for such events would be half the non-zero time, and thus appearing in the wrong part of the spectrum. Most of the single non-zero times were only up to 10 ns later than the zero time. Hence these events do not contribute to events counts at later times in the time spectrum, but would affect the slope of the straight line fitted to the wrap-around region. They only form 0.1% of the total number of neutron events, but were also removed.

Double zero events

In some events both TDC times were recorded as zero. These probably correspond to events at very early times where the TDC is stopped almost as soon as it is started. However, the TDC delays were chosen such that the states of interest did not lie at times close to zero (usually about 50 ns later). Still these were removed as they produced high spikes at zero in the spectrum and were not used in the analysis. They constituted around 2% of the total neutron events.

Overflow events

When an event occurred, all the 12 TDC's were started. But only those TDC's with valid events were stopped by the pulses of those events. All other TDC's were thus not stopped, overflowed and the counts in the last bin were incremented. Since these overflows do not correspond to actual events in that particular detector, they were also rejected.

The overflow counts did not correspond to valid events, so do not affect the efficiencies. But events with a zero time may be valid events. However, the efficiencies were determined from the two peaks in $^{7}Li(p,n)^{7}Be(g.s. + 0.43MeV)$. Since these peaks were recorded at about channel 100, the zero events do not remove valid events from these peaks and the efficiencies are unaffected.

4.4.3 Events not removed

Two types of events could have caused difficulty in the data: events in multiple detectors and events of a low amplitude. Since their contribution to the data of interest was small, and it was difficult to remove them unambiguously, they were not removed from the data.

Events in adjacent detectors

For the detection of the neutrons a stack of 6 detectors was used (section 3.1.2. The reason for using such a modular detector is to obtain a sufficiently large solid angle for the long flight path and to keep the size of each module small enough to get good light collection properties. The neutrons are detected when they scatter off protons or carbon nuclei in the scintillator, which are ionising particles. It can happen that these scattered charged particles travel from one detector into an adjacent detector. Then a single neutron interaction in the detector stack could trigger valid events in more than one detector at a similar time. The delay time between these events would only be the time the charged particles would take to travel from the one to the adjacent detector, which is of the order of 600 ps.

The procedure that was followed for adding spectra was to sum all valid events from all detectors. Then single neutron events would be recorded as multiple neutron events, thus overcounting the neutrons. A better procedure would be to select the event from only *one* detector in the case of a multiple event by, for example, choosing the events with the largest pulse height.

A way to determine the magnitude of this effect is to generate the mean time spectrum for one detector, and then to plot only the mean times of other detectors for events which also occurred in the selected detector (figure 4.6). If no charged scattered particles were to cross the detector walls, then all the other time spectra would be empty. If many particles due to neutron events do cross over into other detectors, then the time spectra of adjacent detectors would have the same structure as the one selected detector.

In figure 4.6, where all the mean time events of detector 3 were plotted, and all multiple events in the other detectors, negligible structure was seen in the adjacent detectors, mainly a low constant background. Since the interest lies in the discrete peaks, there will be no overcounting, and hence no overcalculation of the cross-section in the discrete peaks due to such events. These multiple events could well be cosmic events which had high energy, but did not traverse all 6 detectors.

Hence the procedure that had been followed only produced a small error of ~3% due to overcounting of events, which is negligible compared to the errors of 10-20% from the peak fitting of the spectrum.

Low amplitude events

The neutron events had to pass a threshold in order to be recorded. Many low amplitude pulses from wrap-around neutrons and cosmic muons would be eliminated in this manner. By viewing the amplitude spectrum for each ADC, a software

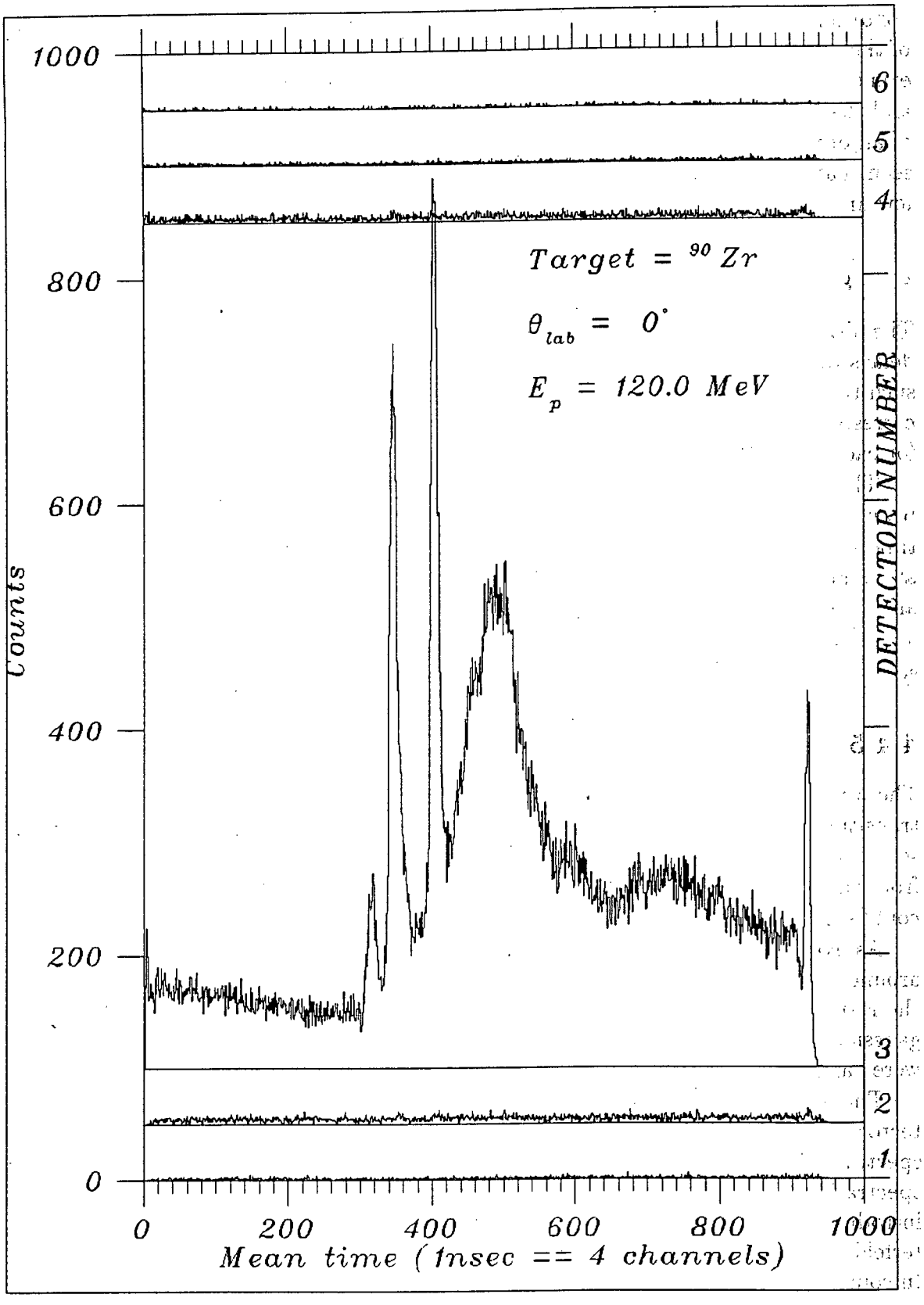

Figure 4.6: *Mean time of events in detector 3 and multiple events in the other detectors.*

threshold was chosen to lie between the cosmic-6 peak and the neutron peak. Using this software threshold further low energy neutron events could be removed. The condition for accepting an event would be that the amplitude pulse from either one of the photomutipliers of one detector would lie above the software threshold. When events were removed in this way, they were less than 1% of the total neutron events and the time spectra of these neutrons had a very similar structure to the spectrum of all other events. Thus it was better not to employ the amplitude cuts. It can be seen that the hardware thresholds had already been effective in removing unwanted low amplitude events.

4.4.4 Combination of spectra

The TDC's were calibrated by recording signals from a pulser and inserting known delays to cover the whole TDC range. Then the calibration factors were calculated such that each time spectrum could be plotted on a common scale where 4 channels correspond to 1 nanosecond. As the mean time spectra were generated, the times for each event had to be multiplied by this measured factor.

The spectra for all runs with the same experimental conditions, ie. same target, beam energy and beam angle, were then summed. During data acquisition, the raw time spectra were shifted by changing delays so that the corresponding peaks lay at roughly the same channel number. For adding the spectra of the 6 detectors and numerous runs, they still had to be shifted more accurately. This was done by aligning the discrete peaks to within one channel. Once added, the statistics of the spectra were much better, and they were then used for peak fitting.

4.4.5 Fitting of mean times

The aim of fitting curves to the spectrum is to extract the number of counts for transitions to different final states, which can be seen as individual peaks, but are in some way superimposed on one another. If all the discrete peaks were well separated from one another, and the background was negligible, then the counts for each peak could simply be found by summing the bins in the region of the peak.

As explained in section 4.4.1, a straight line was fitted to account for the wrap-around neutrons. This straight line was determined and then fixed before fitting the rest of the spectrum. For the discrete states, the GTGR and the $L = 1$ state, gaussian curves were used. The position, width and amplitude of all these curves were varied simultaneously.

The effects which widen the intrinsically narrow states, such as the intrinsic detector resolution and beam time spread, produce a symmetric spread in the time spectra. Thus symmetric gaussians were fitted to the narrow peaks in the time spectra. If certain processes cause asymmetric spreading, then errors would be introduced in the extraction of differential cross-sections for each of the states. Osterfeld, *et al.* [OST 85], performed a microscopic analysis of the $^{90}Zr(p,n)$ spectra. In comparing their calculations to the experimental data, they used a Breit-Wigner form as the shape for the calculated states.

For the GTGR and the states with E_x >15 MeV they chose an asymmetric Breit-Wigner form to fit the data better. The GTGR is a combination of many unresolved narrow states. The shape of this combined peak is not known, but its shape was effectively parameterized by fitting with as few gaussians as possible. In deconvoluting our spectra the GTGR was found to be fitted accurately enough by one or two symmetric gaussians.

Osterfeld [OST 82] strongly criticised the removal of background by fitting a quadratic curve underneath all the discrete states, which has often been done in the analysis of (p,n) data. Osterfeld performed microscopic model calculations of the background underneath the GT resonances of $^{48}Ca(p,n)$ and $^{40}Ca(p,n)$. He found that most of the background for E_x <20 MeV is 1^+ strength.

For 120 MeV, the spectra extend only to E_x ~30 MeV, which is just past the $L = 1$ state. The shape of the continuum cannot be seen and hence quadratic background was fitted towards the higher excitation energy data.

At 160 and 200 MeV, however, where data to higher excitation energy was available, the continuum was fitted in such a way to match the data where no states can be seen, and to fall off to zero before the GTGR. To fit this high excitation energy region a combination of up to four wide gaussian curves was used.

The MINUIT minimisation program [JAM 75, JAM 85] was used for fitting the curves to the spectra. For a set of initial parameters the chi-squared value, ie. the goodness of the fit, was calculated and the MINUIT program then varied the parameters to obtain the smallest chi-squared value within the limits of the parameters. From the fitted parameters the number of events underneath each state were calculated, which were then used to calculate the cross-sections.

The calculation of cross-sections from the number of events of each peak (obtained as described in this chapter above) will be shown in the following chapter. The Gamow-Teller strength calculated for the various transitions will be presented and the sum of the GT strength will be compared to the expected value of the Ikeda sum rule.

Chapter 5

Results and Discussions

The differential cross-sections obtained from the mean time spectra, and the calculations of the Gamow-Teller strengths, will be discussed. The sum of the Gamow-Teller strengths will then be compared to the predictions of the Ikeda sum rule.

5.1 Extracting the cross-sections

The information extracted from the time spectra is the number of counts, N, for each peak. The differential cross-section, in millibarns per steradian, could then be calculated with

$$\frac{d\sigma}{d\Omega} = \frac{N}{\Delta\omega\, n\, t\, \epsilon} \tag{5.1}$$

where N are the number of neutrons detected for a particular transition, $\Delta\omega = 1.18\times10^{-5}$ sr is the solid angle subtended by the stack of detectors, n is the integrated flux of protons on the target, t is the target thickness (=8.98×10^{20} nuclei.cm^{-2} for the ^{90}Zr target) and ϵ is the efficiency of the neutron spectrometer. The value ϵ really is a product of the actual efficiency and the fractional neutron transmission from target to detector. It was determined by Newman [NEW 91] using the reference cross-sections of the $^7Li(p,n)^7Be(g.s.+0.43\ MeV)$. Usually the fractional livetime of the acquisition system is included as a term in equation 5.1. But in our system this was corrected for electronically, by reducing the integrated flux, n (as shown in section 3.3.6).

The error in the differential cross-section was calculated by combining the errors of the parameters in equation 5.1 in quadrature. A particularly large error in the yield was obtained from the MINUIT program when fitting all the peaks simultaneously. This is because the errors on the width and amplitude of the peaks are negatively correlated, and if the error on the peak area is based simply on the errors on width and amplitude, it is thus too large. Moreover the widths of adjacent peaks are strongly negatively correlated. Independent fitting to the IAS only with a linear background resulted in a fractional error of 1–2% for the number of counts. Thus the errors quoted with the calculated cross-sections are overestimates of the actual errors by one order of magnitude. However, uncertainty in the shape of the background introduces systematic errors on peak areas of the order of 10–20%.

In table 5.1 values of the parameters used to calculate the cross-section of the IAS in the 158 MeV zero degree spectrum are listed. The fractional error of the charge was estimated to be about 1%. Note that the fractional error on the number of counts in the table is an overestimate.

Table 5.1: *Sample values and errors for calculating the differential cross-section for the IAS at E_p = 158.4 MeV. Note comments in text regarding the errors quoted in the table.*

Parameter	*Value*	*Error*	*Fractional Error (%)*
charge, Q	14889μC	149μC	1.00
target density, t	134.0 mg.cm^{-2}	0.5 mg.cm^{-2}	0.37
efficiency, ϵ	2.119%	0.024%	1.13
path length, L	174.6 m	0.05 m	0.03
length of detectors	0.6 m	0.005 m	0.83
counts, N	84758	19610	23.15
$d\sigma/d\Omega$	4.20 mb.sr^{-1}	0.98 mb.sr^{-1}	23.22

The deconvoluted zero degree time-of-flight spectra can be seen in figures 5.1, 5.2 and 5.3. The χ^2 value per degree of freedom is shown on each fit, which shows how close the fitted spectrum lies on the data. The interesting features that were fitted in these spectra are (from left to right): three narrow GT ($T = 4$) states, the Fermi IAS ($T = 4$), the wide GTGR ($T = 4$), a GT ($T = 5$) state and an $L = 1$ resonance. The relevant states can be identified by comparing the fitted time spectra to the labelled energy spectrum in figure 2.4.

The best fit was obtained for the 200 MeV data, where $\chi^2/\nu = 2.04$. Each of the discrete peaks fitted well. At each of the energies the fitted curve lies below the data between the states at E_x = 3.0 and 5.1 MeV. In all previous work no state has been reported at this excitation energy. Two possibilities for this discrepancy exist: either a very weak state lies at this energy which has not been detected before, or the background continuum from reactions other than the GT 1^+ transitions extends as far down as E_x = 4 MeV.

Although the GTGR consists of a large number of close states, the number of gaussians utilised to fit it was kept as low as possible. Most of the shape lay very close to a single gaussian, but at the top of the GTGR, additional structure can be seen. At 120 MeV another small gaussian can be used to fit this additional cross-section, but at 200 MeV the data did not lie too far off the fitted curve to require another curve. The best resolution was obtained at 160 MeV , and at this energy the spectra at each of the angles clearly show a double peak at the top. The fraction of cross-section of these two peaks compared to that of the cross-section due to the single gaussian is only about 1.5%, so no additional curves were used to account for them.

The wide gaussians used to fit the continuum follow the data very closely. The

difficulty is in determining how far the continuum stretches towards the lower excitation energies. Under the assumption that most of the strength under the GTGR is GT strength, the continuum was fitted such that it decreased from the data at excitation energies above the $L = 1$ resonance down to the straight line wrap-around at the position of the GTGR. Hence the greatest uncertainty due to this continuum would be caused in the fitted cross-section of the $L = 1$ peak.

The differential cross-section, calculated with equation 5.1 for the zero degree spectra at each of the energies are listed in table 5.2. The cross-section for the Fermi

Table 5.2: *Differential cross-sections for each of the peaks fitted in the mean time spectra. For an explanation of the large cross-section for the $L = 1$ distribution at $E_p = 195.5$ MeV see section 5.1.1. Note comments in text regarding the errors quoted in the table.*

Excitation energy (MeV)		*$d\sigma/d\Omega$ (mb/sr)*		
		E_p=120.0 MeV	E_p=158.4 MeV	E_p=197.5 MeV
1.0	(GT)	1.31±0.60	0.95±0.42	1.08±0.11
2.3	(GT)	4.53±1.00	6.37±0.94	7.52±0.64
3.0	(GT)	2.35±0.74	1.66±0.41	5.05±4.01
5.1	(F)	5.84±1.15	4.20±0.98	4.57±0.69
8.7	(GT)	31.82±4.19	37.36±4.06	50.40±7.78
13.4	(GT)	3.57±1.09	4.53±2.82	5.22±0.44
17.9	(L=1)	12.31±4.27	11.84±6.18	37.02±1.19

state at $E_x = 5.1$ MeV remains fairly constant over the energy range of $E_p = 120$ to 200 MeV. The GT state at $E_x = 1.0$ MeV remains constant, whereas the states at $E_x = 2.3$ and 3.0 MeV increase noticeably. The most dramatic increase with energy is in the GTGR, which rises from 31.82 mb/sr to 50.40 mb/sr. The $T = 5$ state at $E_x = 13.4$ MeV also increases with energy. Again the quoted errors on the differential cross-sections are unreliable, since they do not take proper account of correlations. However, they are of the order of magnitude of the systematic error, which is dominant. A full error analysis remains to be done, but is beyond the scope of this work.

5.1.1 Angular distributions

The strong increase of the cross-section of the transition at 17.9 MeV with increase in angle (shown in figure 5.4 for $E_p = 158.4$ MeV) indicates that this is not an $L = 0$ transition, but probably an $L = 1$ transition. The data shown is for the angles 0°, 2° and 4°. In previous studies this resonance has also been assigned $L = 1$ [BAI 80].

At $E_p = 200$ MeV the angular distributions do not follow the expected trend in the 1991 set of data. The cross-section of the 1^+ states is expected to decrease

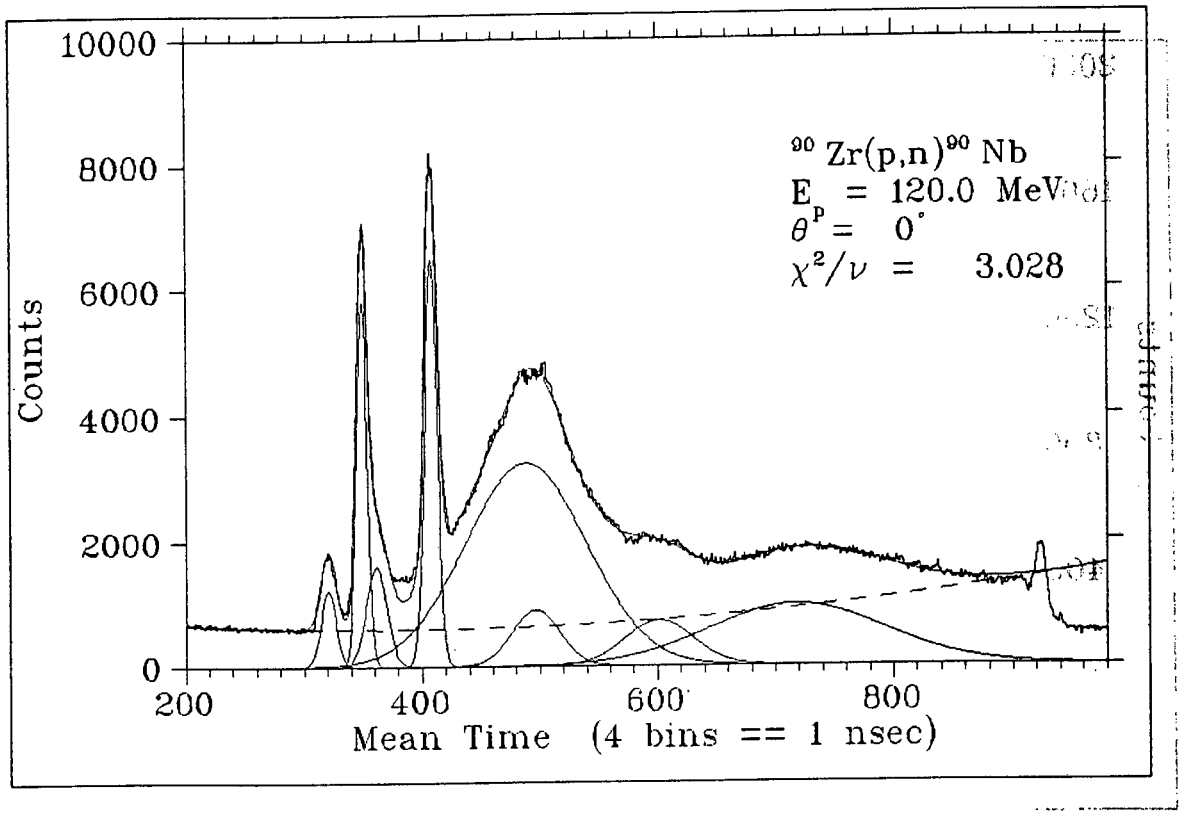

Figure 5.1: *Deconvoluted mean time spectrum at* $E_p = 120.0$ *MeV.*

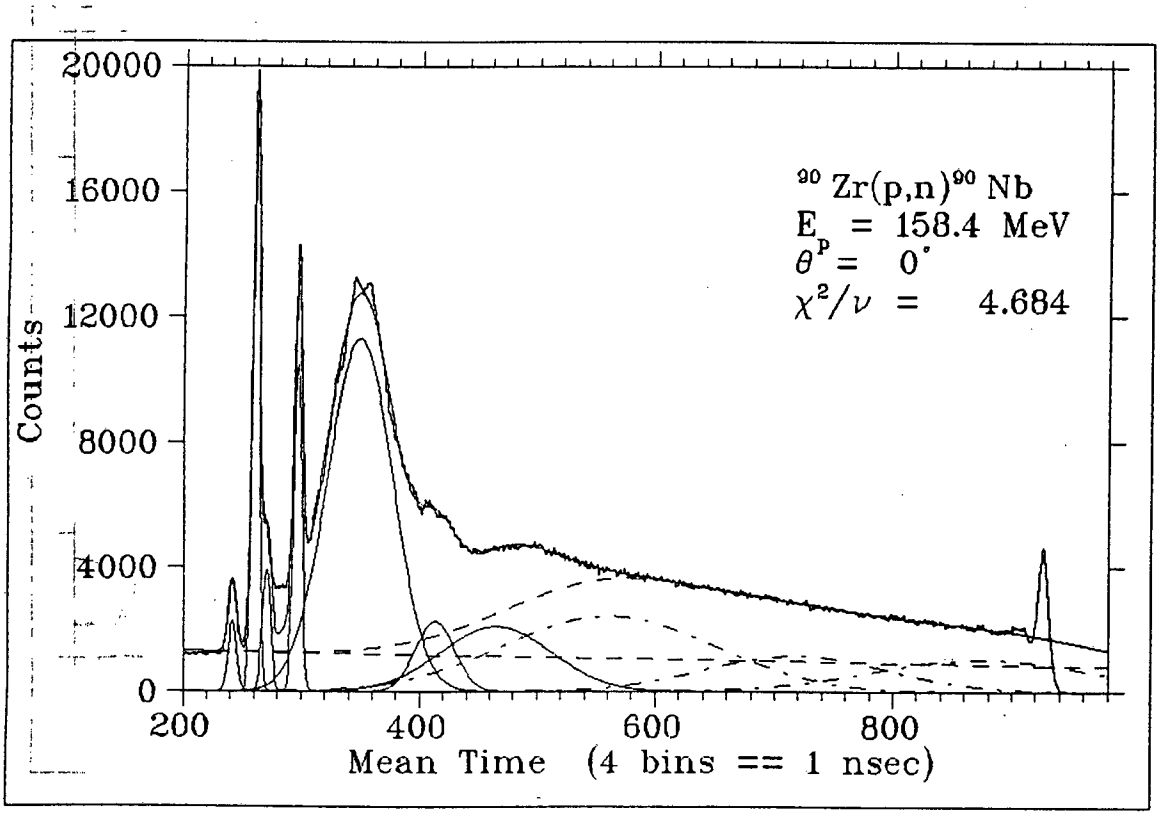

Figure 5.2: *Deconvoluted mean time spectrum at* $E_p = 158.4$ *MeV.*

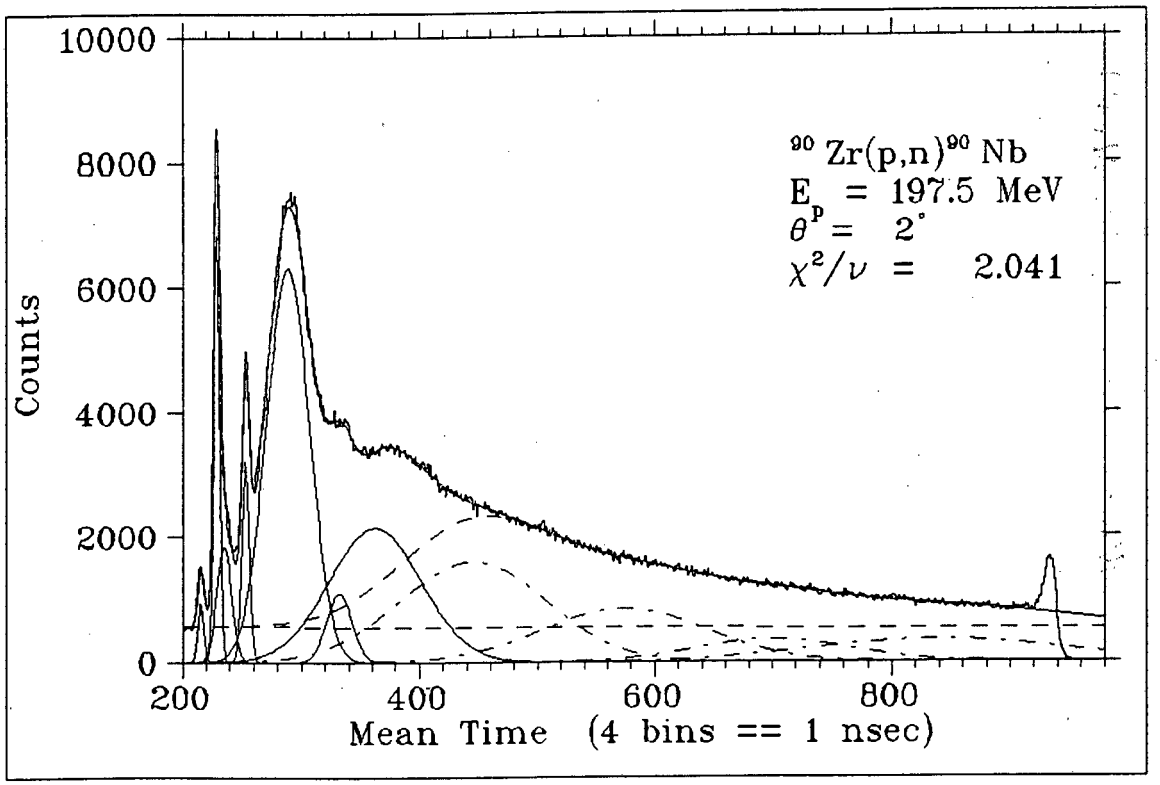

Figure 5.3: *Deconvoluted mean time spectrum at E_p=197.5 MeV. This 2° spectrum was taken as the spectrum closest to the true 0° spectrum (see section 5.1.1).*

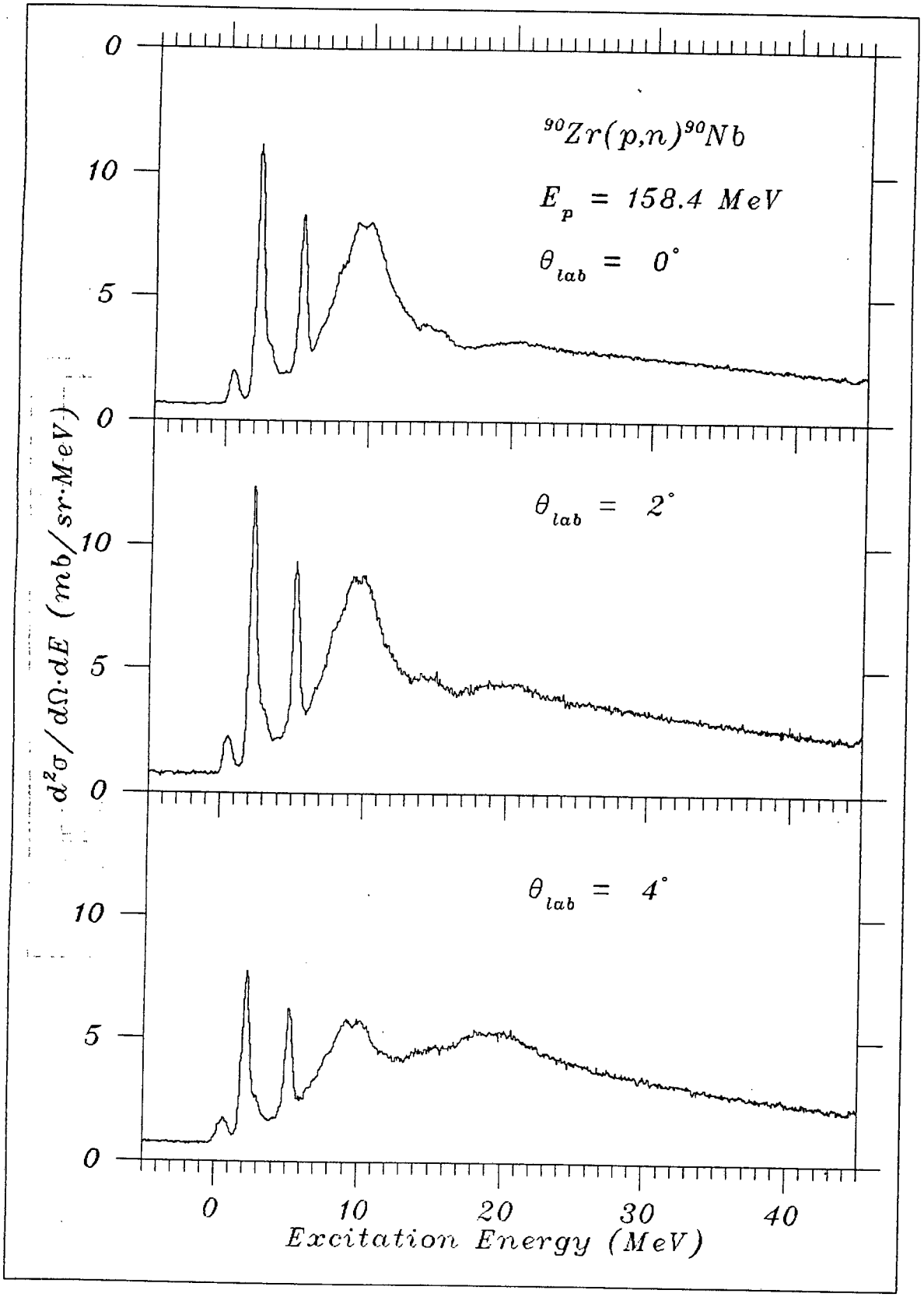

Figure 5.4: *Excitation spectra from the 134 mg.cm^{-2} ^{90}Zr target at E_p = 158.4 MeV showing the angular change of the state at $E_x \sim 20$ MeV from 0° to 4°, indicating this as an $L = 1$ transition.*

with increasing angle, but it increases from 0° to 2°, and then decreases from 2° to 4°. The $L = 1$ peak cross-section is expected to increase from 0° to 4°, but it decreases from 0° to 2°, and only then increases from 2° to 4°. These spectra were compared to a set of runs in the previous year, using the thinner ^{90}Zr target, where the angular distributions were as expected. It was concluded that the true 0° spectrum lies *closest* to the measured 2° spectrum. In table 5.2 the $L = 1$ cross-section is significantly larger at 200 MeV, which may be a result of the 2° spectrum being noticably different from the true 0° spectrum.

It is suspected that the angle settings of the beam swinger were set incorrectly for the 200 MeV runs in June 1991. Hence the $E_p = 197.5$ MeV, 2° spectrum was used in comparison with the 0° degree spectra at other energies. The (p,n) spectra of other targets at the dubious angular setting were examined. The same trend as for ^{90}Zr , with the $L = 1$ peak being lowest at 2°, was observed for all the other targets, thus confirming the suspicion that the beam swinger angles had been incorrectly set.

5.2 Gamow-Teller strengths

The GT strength, $B(GT)$, for each GT transition can be calculated using equation 2.22. Then the GT strength can be summed for all the discrete states, which gives the total observed GT strength. This sum was compared to the value of 30, from the Ikeda Sum Rule and in table 5.3 the fraction of the sum rule observed is shown.

Table 5.3: *Fraction of GT strength in* $^{90}Zr(p,n)^{90}Nb$. *The sum of GT is lower at* $E_p \sim 200$ *MeV, possibly because the detection angle was not quite zero degrees. Note comments in text regarding the errors quoted in the table.*

Proton Energy	$\Sigma B(GT)$	*GT fraction*
(MeV)		*%*
120.0	15.7±3.5	52.3±11.6
158.4	14.6±3.7	48.7±12.4
197.5	11.8±2.3	39.2± 7.7

The errors on $\Sigma B(GT)$ and the *GT fraction* derive from the errors on the cross-section of the GT states and the IAS, and hence may be unreliable. The sum of the GT strength for $E_p = 120$ and 160 MeV lies at 50% of the sum rule value within the errors. The lower value of the $\Sigma B(GT)$ for $E_p = 200$ MeV most likely arises from the error in the angle settings at this energy: even though the 2° spectra is closest to 0°, it is most likely not *exactly* at 0°. Hence the measured GT cross-sections, which are $L = 0$ transitions peaked at 0°, are lower than at the true 0° setting, which causes the sum of the GT strength for the 200 MeV data to be reduced.

Chapter 6

Conclusions

The total GT strength measured in this experiment will be related to the sum obtained in other studies. Recommendations for further investigation will be given.

6.1 Missing GT strength

The strength which has been extracted from the ^{90}Nb spectra was for the discrete GT states and the GTGR. The strength from these states provides a lower limit to the strength expected from the sum rule. The missing strength has to be accounted for, or an explanation found why the total strength was not detected.

In figure 6.1 the fraction of GT sum rule strength observed for (p,n) on many nuclei can be seen. The hatched region indicates the uncertainty of how much GT

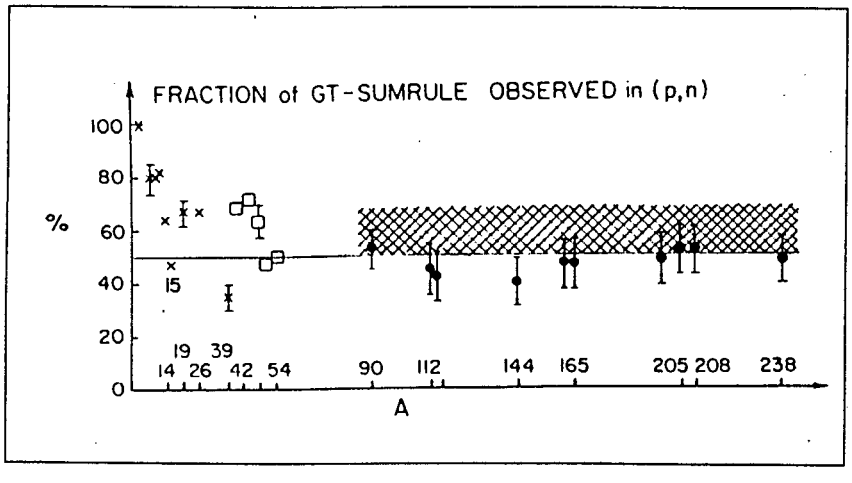

Figure 6.1: *The fraction of the GT sum rule observed in (p,n) reaction on many nuclei. The hatched area includes strength underneath the discrete peaks, but not at excitation energies above the GTGR. From [GAA 85].*

strength lies in the background underneath the discrete states. The summed GT strength does not include strength in the continuum. It can be seen that our summed

GT strength of around 50±12 % of the Ikeda sum rule is in accordance with the sum obtained for many other nuclei with $A \geq 90$.

The (p,n) reaction probes the $S_{\beta-}$ strength. In sections 2.1 and 2.4 it was stated that the $S_{\beta+}$ strength can be obtained using the (n,p) reaction. Recent data by Olsson, *et al.* [OLS 92] using $^{90}Zr(n,p)$ at $E_n = 98$ MeV, showed that the sum rule strength obtained from the GT 0° cross-section is

$$S_{\beta+} = 1.7 \pm 0.2 \text{ units} .$$

This value is small compared to the $3(N-Z) = 30$ for ^{90}Zr, but it means that even a larger fraction of the $S_{\beta-} = 3(N-Z) + S_{\beta+}$ strength has remained undetected.

Many suggestions have been made that a large proportion of the strength has shifted into the high excitation energy continuum. Possible processes for this could be Δ-hole or 2p-2h excitations, as described in section 2.6.

In the continuum it becomes extremely difficult to extract the additional GT ($L = 0$) strength. The states at high excitation energy become very broad and flat, so they cannot be identified clearly. There are also a large number of states which overlap substantially. For higher excitation energy other processes also contribute to the spectrum. The shape of the background due to these other processes is not understood well, and no models can so far describe it accurately enough that it can be subtracted and the GT strength identified. The phenomelogical model by Kalbach, using multistep-direct-reactions can be used to obtain an estimate of the events due to reactions other than GT ($L = 0$) transitions. However, this model does not describe the processes — it is simply a model that is able to fit the experimental angular distributions extremely well. Usually quasi-free scattering calculations have been used to account for reactions apart from (p,n) in the background (section 2.6).

6.2 Further experimental work

A possible method for analysing the continuum is to perform a multipole decomposition of events within a narrow excitation energy band. For this measurements at a large number of angles in the range 0° to 25° are necessary, which have so far not become available from our experiments at NAC. If such data becomes available, this method can be used to extract the $L = 0$ component of the continuum, and then we could obtain a measure of how much of the strength can be accounted for in the continuum.

In future experiments the overall energy resolution can be improved by positioning the detector stack longitudinally to the neutron beam so that the position of the neutron interaction in the detector can be determined more accurately. However, it must then be ensured that contributions from other errors, such as the beam time width and the energy spread in the target (section 3.2) are less important than that of the improved path length uncertainty.

These studies on ^{90}Zr, on which much published data is available, have been a confirmation to us that our neutron spectrometer at NAC can be used to obtain reliable data. The next phase of the experimental program would be to study odd-A nuclei.

Finally, the missing strength leads to the question: has the GT strength just not been identified in the experiment, or are other physical processes involved, removing the strength, which we do not (so far) understand? In the midst of much experimental and theoretical work this question still remains open.

I will conclude with the comment made by Osterfeld in a recent review paper on nuclear spin and isospin excitations [OST 92]:

> "This history of spin and isospin excitations in nuclei over the last decade indicates that still more unexpected phenomena await discovery and that nuclear physics will continue to be challenging and exciting."

Appendix A

Log of the ^{90}Zr data

The runs 150–330 were performed during October/November 1990. The runs 510–637 were performed during June/July 1991. The short Lithium runs (in between the longer runs on Zirconium) used for efficiency calculations have not been listed in the table.

Note that θ_{beam} is the beam swinger angle (the angle of the deflected proton beam with respect to its undeflected position), θ_{target} is the rotation angle of the target w.r.t. the undeflected proton beam. During the 1990 runs, the experiment was run with a second parasitic experiment, which required the rotation of the target.

Table A.1: *The log of the ^{90}Zr data.*

Run number	*File size*	E_p (MeV)	θ_{beam} (deg)	*Charge* (μC)	*Run date*	*Run time*	*Beam* (nA)	θ_{target} (deg)	*Thickness* $(mg.cm^{-2})$
150	821	200.0	0	2875	19-10-90	7:11	108	30	10.0
160	604	200.0	0	636	20-10-90	0:54	200	30	10.0
162	2083	200.0	0	2999	20-10-90	4:11	200	30	10.0
177	825	200.0	0	1662	21-10-90	2:19	201	30	10.0
178	3269	200.0	0	3801	21-10-90	6:01	197	30	10.0
184	244	198.4	0	1276	26-10-90	1:40	225	30	10.0
186	82	198.4	4	386	26-10-90	0:32	205	30	10.0
187	9	198.4	4	38	26-10-90	0:04	200	30	10.0
188	15	198.4	4	71	26-10-90	0:06	200	30	10.0
189	115	198.4	4	545	26-10-90	0:47	200	30	10.0
190	61	198.4	4	296	26-10-90	0:24	200	30	10.0
192	371	198.4	4	1804	26-10-90	2:25	200	30	10.0
193	125	198.4	4	593	26-10-90	0:49	230	30	10.0
202	470	198.4	4	2195	27-10-90	3:02	205	30	10.0
205	8	198.4	2	21	27-10-90	0:03	201	30	10.0

Run number	*File size*	E_p (MeV)	θ_{beam} (deg)	*Charge* (μC)	*Run date*	*Run time*	*Beam* (nA)	θ_{target} (deg)	*Thickness* $(mg.cm^{-2})$
206	913	198.4	2	2785	27-10-90	3:55	201	30	10.0
224	15	198.4	0	57	28-10-90	0:05	200	30	10.0
225	627	198.4	0	2788	28-10-90	3:52	210	30	10.0
299	532	199.6	2	3175	18-11-90	4:21	210	0	10.0
326	421	121.1	0	779	24-11-90	4:25	498	0	10.0
328	100	121.1	0	1854	24-11-90	1:04	507	0	10.0
330	287	121.1	0	5413	24-11-90	3:04	502	0	10.0
511	86	197.5	0	59	21-06-91	0:05	197	0	134.
513	2258	197.5	0	2906	21-06-91	4:04	200	0	134.
525	3080	197.5	0	2409	22-06-91	3:19	205	0	134.
526	594	197.5	0	486	22-06-91	0:40	215	0	134.
530	3714	197.5	0	2832	22-06-91	4:00	200	0	134.
533	51	197.5	2	37	22-06-91	0:03	210	0	134.
534	1585	197.5	2	1165	22-06-91	1:38	213	0	134.
536	4794	197.5	2	3518	23-06-91	4:59	215	0	134.
546	2714	197.5	4	2051	23-06-91	3:01	203	0	134.
555	2169	158.4	0	2292	28-06-91	1:25	517	0	134.
557	2091	158.4	0	2254	28-06-91	1:21	500	0	134.
564	5075	158.4	0	4404	28-06-91	2:43	460	0	134.
569	4292	158.4	2	4027	28-06-91	2:27	500	0	134.
579	3773	158.4	2	3097	29-06-91	1:58	476	0	134.
591	6117	158.4	4	6192	30-06-91	3:39	509	0	134.
594	1846	158.4	0	1642	30-06-91	0:58	495	0	134.
598	3870	158.4	0	3611	30-06-91	2:06	513	0	134.
599	1546	158.4	0	1457	30-06-91	0:49	524	0	134.
606	3333	120.0	0	6668	05-07-91	3:52	504	0	134.
617	3072	120.0	0	6157	06-07-91	3:30	507	0	134.
623	527	120.0	2	1071	06-07-91	0:35	503	0	134.
625	2572	120.0	2	5258	06-07-91	3:01	502	0	134.
637	2437	120.0	4	5303	08-07-91	3:02	495	0	134.

Table A.2: *Run numbers for the summed ^{90}Zr spectra displayed in the thesis. Data for very short runs and for runs with very unstable beam time were not used in the summing. For spectra not on this list, the runs numbers are shown on the figure.*

E_p (MeV)	θ_{beam} (deg)	*Run numbers*
120.0	0	606, 617
120.0	2	623, 625
120.0	4	637
158.4	0	555, 557, 564, 594, 598, 599
158.4	2	569
158.4	4	591
197.5	0	525, 526, 530
197.5	2	534, 536
197.5	4	546

Bibliography

[ALV 38] L.W.Alvarez, Phys.Rev. **54** (1938) 609.

[ALV 87] L.W.Alvarez, *ALVAREZ: adventures of a physicist*, Basic Books Inc. Publ., New York (1987).

[AND 85] B.Anderson, *et al.*, Phys.Rev.C **31:4** (1985) 1161.

[AND 90] B.Anderson, *et al.*, Phys.Rev.C **41:4** (1990) 1474.

[BAI 80] D.E.Bainum, *et al.*, Phys.Rev.Lett **44** (1980) 1751.

[BER 81] G.F.Bertsch, Nucl.Phys. **A354** (1981) 157.

[BER 82] G.F.Bertsch, *et al.*, Phys.Rev.C **25** (1982) 804.

[BER 87] G.F.Bertsch, *et al.*, Rep.Prog.Phys. **50** (1987) 607.

[BLA 76] M.Blann, *et al.*, Nucl.Phys. **A257** (1976) 15.

[BRE 87] T.Bressani *et al.*, in *Hadronic Physics at Intermediate Energy, 2*, ed. T.Bressani, B.Minetti and G.Pauli, North-Holland (1987).

[CHA 81] D.Cha, *et al.*, Phys.Rev.C **24:2** (1981) 533.

[CON 92] L.Conradie, NAC, private communication, 1992.

[DAG 81] D'Agostini, *et al.*, NIM **185** (1981) 49.

[DOE 75] R.R.Doering, *et al.*, Phys.Rev.Lett **35** (1975) 1691.

[DRO 86] S.Drożdż, *et al.*, Phys.Lett. **166B:1** (1986) 18.

[FIR 79] F.W.K.Firk, NIM **162** (1979) 539.

[FRI 85] D.L.Friesel, *et al.*, NIM B **10-11** (1985) 864.

[FUJ 64] J.I.Fujita *et al.*, Phys.Rev. **133** (1964) B549.

[GAA 80] C.Gaarde, *et al.*, Nucl.Phys. **A334** (1980) 248.

[GAA 81] C.Gaarde, *et al.*, Nucl.Phys. **A369** (1981) 258.

[GAA 85] C.Gaarde, in *Proceedings of the Niels Bohr Centennial Conference on Nuclear Structure*, Copenhagen, (North-Holland) (1985).

[GOO 79] C.D.Goodman, IEEE Trans. on Nucl.Sci. **26** (1979) 2248.

[GOO 80] C.D.Goodman in *The (p,n) reaction and the Nucleon-Nucleon Force*, ed. C.D.Goodman, *et al.*, Plenum Press (1980).

[GOO 84] C.D.Goodman, Prog. in Part. and Nucl. Phys. **11** (1984) 475.

[GOO 87] C.D.Goodman, *et al.*, Can.J.Phys. **65** (1987) 549.

[GOU 80] C.A.Goulding, *et al.*, Phys.Rev.Lett. **44:26** (1980) 1755.

[HOR 75] D.J.Horen *et al.*, Nuclear Data Sheets **16:1** (1975).

[HOR 81] D.J.Horen *et al.*, Phys.Lett. **99B:5** (1981) 383.

[IKE 63] K.I.Ikeda *et al.*, Phys.Lett. **3** (1963) 271.

[JAM 75] F.James and M.Roos, Computer Physics Communications **10** (1975) 343.

[JAM 85] F.James and M.Roos, CERN Computer Centre Program Library **D506** (1985).

[KAB 90] R.T.Kabutz, *Timing measurements for the (p,n) "Time of flight" experiment*, UCT Honours project (1990), unpublished.

[KER 59] A.K.Kerman, *et al.*, Ann.of Phys. **8** (1959) 551.

[KRM 80] F.Krmpotić, *et al.*, Nucl.Phys. **A342** (1980) 497.

[LOV 81] W.G.Love, *et al.*, Phys.Rev.C **24:3** (1981) 1073.

[LOV 87] W.G.Love, *et al.*, Can.J.Phys. **65** (1987) 536.

[MAD 83] R.Madey, *et al.*, NIM **214** (1983) 401.

[MAT 83] G.J.Mathews, *et al.*, Phys.Rev.C **28:3** (1983) 1367.

[MUT 85] K.Muto, *et al.*, Phys.Lett.**165B:1,2,3** (1985) 25.

[NAC 87] NAC/AR/87-01, NAC Annual Report, June 1987.

[NAC 89] NAC/AR/89-01, NAC Annual Report, June 1989.

[NAC 90] NAC/AR/90-01, NAC Annual Report, June 1990.

[NAC 91] NAC/AR/91-01, NAC Annual Report, June 1991.

[NAK 82] K.Nakayama, *et al.*, Phys.Lett. **114B:4** (1982) 217.

[NEW 91] R.T.Newman, M.Sc. Thesis, University of Cape Town, 1991.

[OLS 92] N.Olsson, *et al.*, Nucl.Phys. **A545** (1992) 785.

[OST 82] F.Osterfeld, Phys.Rev.C **26:2** (1982) 762.

[OST 85] F.Osterfeld, *et al.*, Phys.Rev.C **31:2** (1985) 372.

[OST 92] F.Osterfeld, Reviews of Mod. Phys. **64:2** (1992) 491.

[PRE 68] B.M.Preedom, *et al.*, Phys.Rev. **166:4** (1968) 1156.

[RHO 74] M.Rho, Nucl.Phys. **A231** (1974) 493.

[SCH 83] O.Scholten, *et al.*, Phys.Rev.C **27:6** (1983) 2975.

[SCO 90] W.Scoble, *et al.*, Phys.Rev.C **41:5** (1990) 2010.

[SHI 74] K.Shimizu, *et al.*, Nucl.Phys. **A226** (1974) 282.

[TAD 81] T.N.Taddeucci, *et al.*, Phys.Rev.C **25:2** (1981) 1094.

[TAD 86] T.N.Taddeucci, *et al.*, Phys.Rev.C **33:2** (1986) 746.

[TAD 87] T.N.Taddeucci, *et al.*, Nucl.Phys. **A469** (1987) 125.

[TSH 92] V.M.Tshivhase, M.Sc. Thesis. University of Cape Town, 1992.

[WAT 83] J.W.Watson, *et al.*, NIM **215** (1983) 413.

[WAT 89] J.W.Watson, Phys. Rev. C **40.** (1989) 22.

[WIL 80] H.S.Wilson, *et al.*, Phys.Rev.C **22** (1980) 1696.

[WIL 82] D.H.Wilkinson, Nucl.Phys. **A377** (1982) 474.

[WON 90] S.S.M.Wong, *Introductory Nuclear Physics*, Prentice-Hall International (1990).

[ZAF 80] C.D.Zafiratos in *The (p,n) reaction and the Nucleon-Nucleon Force*, ed. C.D.Goodman, *et al.*, Plenum Press (1980).